Sea-ice and water dynamics and moonlight impact the acoustic backscatter diurnal signal over the eastern Beaufort Sea continental slope

Igor A. Dmitrenko[1], Vladislav Petrusevich[1], Gérald Darnis[2], Sergei A. Kirillov[1], Alexander S. Komarov[3], Jens K. Ehn[1], Alexandre Forest[2], Louis Fortier[2], Søren Rysgaard[1,4] and David G. Barber[1]

[1]Centre for Earth Observation Science, University of Manitoba, Winnipeg, R3T 2N2, Canada
[2]Department of Biology, Laval University, Québec City, G1V 0A6, Canada
[3]Data Assimilation and Satellite Meteorology Research Section, Environment and Climate Change Canada, Ottawa, K1G 3Z4, Canada
[4]Arctic Research Centre, Aarhus University, Aarhus, DK-8000, Denmark

Correspondence to: Igor A. Dmitrenko (igor.dmitrenko@umanitoba.ca)

Abstract. A two-year-long time series of currents and acoustic backscatter from an Acoustic Doppler Current Profiler, moored over the eastern Beaufort Sea continental slope from October 2003 to September 2005, were used to assess dynamics and variability of the sound-scattering layer. It has been shown that acoustic backscatter is dominated by a synchronized diel vertical migration (DVM) of the zooplankton. Our results show that DVM timings (i) were synchronous with sunlight, and (ii) were modified by moonlight and sea-ice, which attenuates light transmission to the water column. Moreover, DVM is modified or completely disrupted during highly energetic current events. Thicker ice observed during winter-spring 2005 lowered the backscatter values, but favored extending DVM toward the midnight sun. In contrast to many previous studies, DVM occurred through the intermediate water layer during the ice-free season of the midnight sun in 2004. In 2005, the midnight sun DVM was likely impacted by a high acoustic scattering generated by suspended particles. During full moon at low cloud cover, the nighttime moonlight illuminance led to zooplankton avoidance of the sub-surface layer disrupting DVM. Moreover, DVM was disrupted by upwelling, downwelling and eddy passing. We suggest that these deviations are consistent with DVM adjusting to avoid enhanced water dynamics. For upwelling and downwelling, zooplankton likely respond to the along-slope water dynamics dominated by surface- and depth-intensified flow, respectively. This drives zooplankton to adjust DVM by aggregating in the low or upper intermediate water layer for upwelling and downwelling, respectively. The baroclinic eddy reversed DVM below the eddy core.

1 Introduction

The acoustic backscatter signal recorded in the ocean by acoustic Doppler current profilers (ADCPs) is mainly dominated by zooplankton. The diurnal patterns of the acoustic backscatter signal are comprised of diel vertical migration (DVM) of zooplankton, the synchronized movement of zooplankton up and down in the water column over a daily cycle (e.g., Brierley, 2014). In terms of biomass, DVM is arguably the largest daily migration of animals on earth (Hays, 2003), and the largest non-human migration (Brierley et al., 2014). DVM has been extensively explored in the Arctic using either echo sounders or zooplankton nets (e.g., Kosobokova, 1978;

Fortier, et al., 2001; Blachowiak-Samolyk et al., 2006; Cottier et al., 2006; Falk-Petersen et al., 2008). The latest progress in assessing DVM in the Arctic is related to understanding DVM during the Arctic polar night (Berge et al., 2009, 2015) and the role of moonlight in modifying DVM (Last et al., 2016; Petrusevich et al., 2016). While significant progress has been achieved in understanding DVM, the sea-ice and ocean dynamics control on DVM in the Arctic environment remains poorly appreciated.

ADCPs moored over the entire annual cycle in the seasonally ice-covered Arctic water provide a unique temporal evolution of the DVM patterns. This seasonal perspective is essential to achieve a more complete and quantitative understanding of DVM in response to the light and sea-ice conditions (e.g., Tran et al., 2016; Hobbs et al., 2018). Here we assess temporal evolution of the DVM patterns using a two-year-long time series of velocity and acoustic backscatter from an ADCP-equipped mooring deployed over the upper eastern Beaufort Sea continental slope from October 2003 to September 2005 (Figure 1). The ADCP limitation, however, comes from its ability to detect only the biomass moving at a population level, i.e., comprising the migrating sound-scattering layer (Hobbs et al., 2018).

The oceanographic factors controlling DVM in the seasonally ice-covered Arctic areas, located at the inner border of the polar circle, remains poorly assessed. Here we use observations from the oceanographic mooring located at ~71°N, the area, where the Sun is between 0 and <6° below the horizon all day on the winter solstice. At this latitude no actual daylight is experienced during short winter daylight hours with the exception of civil twilight when solar illumination is still sufficient for the human eye to distinguish terrestrial objects. This geographical position makes our DVM observational site vastly different from those at Svalbard (astronomical twilight, the Sun is between 12 and 18° below the horizon, ~80°N; e.g., Grenvald et al., 2016; Darnis et al., 2017), Canada Basin (nautical twilight, the Sun is between 6 and 12° below the horizon, ~77.5°N; La et al., 2018), and Northeast Greenland (nautical twilight, ~74.5°N, Petrusevich et al., 2016). Civil twilight is observed at the CA13 latitude from 19 November to 21 January. For the winter solstices (22 December), the civil twilight lasts for about 3 h. The polar day (or the midnight sun, the Sun is above the horizon for the entire 24 hours) lasts at the CA13 latitude from 10 May to 1 August.

This study is built on results by Dmitrenko et al. (2018) on water dynamics over the eastern Beaufort Sea continental slope taking advantage of using the ADCP-derived acoustic backscatter for temporal appreciation of DVM patterns during two consecutive annual cycles. Our particular focus is on the DVM modifications, caused by wind-forced upwelling and downwelling over the Beaufort Sea continental slope, and the different types of sea-ice cover. We also add more data points and further proof to research focused on the effect of moonlight on DVM (e.g., Webster et al., 2015; Last et al., 2016; Petrusevich et al., 2016).

2 Data

We used data from the ArcticNet oceanographic mooring CA13 deployed over the upper Canadian Beaufort Sea continental slope at 300-m depth from 9 October 2003 to 4 September 2005 at 71°21.356'N, 131°21.824'W (Figure 1). The mooring description can be found in Dmitrenko et al. (2016). For this study, we used (i) velocity and acoustic backscatter intensity records from a 300 kHz upward-looking Workhorse Sentinel ADCP by Teledyne RD Instruments (RDI) at 119-m depth and (ii) temperature records from the moored CTD (conductivity-temperature-depth) SBE-37 by Sea-Bird Electronics, Inc. at 49-m and 119-m depth. The velocity and acoustic backscatter data were obtained at 8-m depth intervals, with a 1-h ensemble time interval and 30 pings per

ensemble. The first bin was located at ~9 m above the transducer, i.e., at 108 m depth. For this research, we used bins at 28, 68, and 108 m depth. Data at 48 and 88 m depth were obtained by linear interpolation between bins at 44 m and 52 m, and 84 m and 92 m, respectively. The RDI ADCP precision and resolution are ± 0.5% and ± 0.1 cm s^{-1}, respectively. The standard deviation for an ensemble average of 30 pings for the 8-m depth cell size is reported by RDI to be 1.19 cm s^{-1}. The accuracy of the ADCP vertical velocity measurements is not validated; however, for the 600 kHz RDI ADCP, Wood and Gartner (2010) reported that the vertical velocity is more accurate than the horizontal velocity by at least a factor of two. The compass accuracy is ± 2°. The magnetic deviation was added. The along-slope direction was determined to be 64°T (°T - the direction measured with reference to the true north) using the scatterplot of the daily mean velocity data following an assumption that the maximum dispersion of velocity measurements occurs along the continental slope (Dmitrenko et al., 2016). Mooring data were complemented by the vertical CTD, chlorophyll fluorescence and particulate beam attenuation profiles taken at mooring deployment and recovery in October 2003 and September 2005, respectively, and in July 2004 using a CTD probe SBE-911 (Figure 2). According to the manufacturers' estimates, individual temperature and conductivity measurements are accurate to ±0.001°C and ±0.0003 S m^{-1}, respectively, for the SBE-911, and to ±0.002°C and ±0.0003 S m^{-1} for SBE-37.

The total cloud cover (%) for the mooring location is obtained from the National Centers for Environmental Prediction - NCEP (Kalnay et al., 1996). The accuracy of the cloud cover data is uncertain. Comparing the satellite- to NCEP-derived cloud cover over the Arctic (60°-90°N) for 2000-2014 shows that NCEP data underestimates the mean cloud cover amount by about 25-30% all year round (Liu and Key, 2016).

For sea-ice, we use the following five different data sets. (i) Sea-ice concentrations (Figure 3b) are derived from the Advanced Microwave Scanning Radiometer for EOS (AMSR-E) with errors less than 10% for ice concentrations above 65% (Spreen et al., 2008). They have been computed by applying the ARTIST Sea Ice (ASI) algorithm to brightness temperatures measured with the 89 GHz AMSR-E channels and are available through https://icdc.cen.uni-hamburg.de/en/seaiceconcentration-asi-amsre.html. The ASI algorithm is described in Spreen et al. (2008). The spatial grid resolution for ice concentration is 6.25 km, and we used data from the pixel, closest to the mooring position.

For sea ice thickness, we used (ii) grid daily data from the Pan-Arctic Ice Ocean Modeling and Assimilation System (PIOMAS, http://psc.apl.uw.edu/research/projects/arctic-sea-ice-volume-anomaly/data/) developed at the Polar Science Center, University of Washington. PIOMAS is a coupled ocean and sea ice model that assimilates daily sea-ice concentration and sea surface temperature satellite products (Zhang and Rothrock, 2003). We used data from the grid node at 71.3°N, 133.3°W closest to the mooring position. Schweiger et al. (2011) reported, that PIOMAS spatial thickness patterns agree well with Ice, Cloud, and land Elevation Satellite (ICESat) thickness estimates (also used in this study) with pattern correlations of above 0.8. However, PIOMAS tends to overestimate thicknesses for the thin ice area around the Beaufort Sea, and underestimate the thick ice area around northern Greenland and the Canadian Arctic Archipelago (Wang et al., 2016). The overall differences between PIOMAS and ICESat is -15% or -0.31 m (Wang et al., 2016). As an alternative source of sea-ice thickness data, we used (iii) simulations based on the Hybrid Coordinate Ocean Model (HYCOM, v2.2.98; e.g. Chassignet et al., 2007) + Community Ice Code (CICE, v4.0; e.g. Hunke, 2001) coupled ocean and sea ice system, developed at the Danish Meteorological Institute (DMI, Madsen et al., 2016). The horizontal resolution is ~10 km. The model domain covers the Arctic Ocean and the Atlantic Ocean down to ~20°S. Madsen et al. (2016) reported that the

simulated sea-ice thickness distribution near the Canadian Arctic Archipelago and the northern coast of Greenland is consistent with CryoSat-2 satellite measurements and the NASA Operation IceBridge airborne observations. Simulated sea-ice thicknesses, shown in Figure 3b, were derived for the grid node closest to the mooring position. Spatial distributions of sea-ice thickness (Figures 4, 6e, and 6f) were acquired from http://ocean.dmi.dk/arctic/icethickness/thk.uk.php.

(iv) We also used data on sea-ice thickness from ICESat obtained from the NASA National Snow and Ice Data Center – NSIDS (Yi and Zwally, 2009). Data represent the gridded 25-km means. Kwok et al. (2007) found a mean uncertainty of the sea-ice thickness of about 0.7 m, and the sea-ice draft estimated from ICESat data relative to that measured at moorings agreed within 0.5 m. We use data from the ICESat campaigns previously used by Kwok et al. (2009): ON03 (24 September - 18 November 2003), FM04 (17 February – 23 March 2004), ON04 (3 October – 8 November 2004), and FM05 (17 February – 24 March 2005) shown in Figure 5. Finally, we used (v) satellite synthetic aperture radar (SAR) imagery acquired by Canadian RADARSAT over the mooring location before the sea-ice breakup in 2004 and 2005 (Figures 6a-6d). RADARSAT data were acquired through the Government of Canada's Earth Observation Data Management System (https://www.eodms-sgdot.nrcan-rncan.gc.ca).

Snow depth over sea-ice, derived from AMSR-E/Aqua, was obtained from NSIDC (Cavalieri et al., 2014). The 12.5 km snow depth is provided as a 5-day running average. It is generated using the AMSR-E snow-depth-on-sea-ice algorithm based on the spectral gradient ratio of the 18.7 GHz and 36.5 GHz vertical polarization channels (Markus and Cavalieri, 1998). As of the AMSR-E sea-ice concentrations, for generating time series of the snow depth over sea-ice (Figure 3a) we used data from the pixel closest to the mooring position.

3 Methods

We analyzed the acoustic backscatter and velocity time series from ADCP to reveal modifications of the acoustic backscatter diurnal signal primarily dominated by DVM. In general, the particles in the water column producing a significant portion of acoustic backscatter comprise suspended sediments or planktonic organisms (e.g., Petrusevich et al., 2020). Frazil ice crystals also generate an enhanced acoustic backscatter (e.g., Dmitrenko et al., 2010). However, sound scattering produced by zooplankton is more complex compared to that generated by sediment particles due to DVM (Stanton et al., 1994). Moreover, ADCPs, unlike echo-sounders, are limited in deriving accurate quantitative estimates of zooplankton biomass (Lemon et al., 2001, 2012; Vestheim et al., 2014). This is mainly due to calibration issues (Brierley et al., 1998; Fielding et al., 2004; Lemon et al., 2008; Lorke et al., 2004) and the beam geometry (Vestheim et al., 2014). To account for the beam geometry, we derived mean volume backscatter strength (MVBS) in dB from the acoustic backscatter echo intensity following the procedure described by Deines (1999).

Using vertical velocity for DVM interpretation is not intuitive. The vertical velocity component is very sensitive to spatial inhomogeneity of the flow field and errors in the ADCP tilt angle, introducing errors and significant contamination to the measured vertical velocity component (Ott, 2005). Deviations of the vertical velocity diurnal pattern can also be attributed to a more dynamical (turbulent) state of the environment associated with high-velocity currents. In what follows, we are only interested in the vertical velocity estimates, which are sensitive to the MVBS diurnal cycling. For this analysis, the vertical velocity time series were filtered as following. We removed diurnal cycling and low frequency variability using 24-hour and 90-day running mean,

respectively. All velocity values exceeding one standard deviation of the mean for the residual time series are considered as noise attributed to spatial inhomogeneity of the flow field and errors in the ADCP tilt angle. In what follows, we show that the contaminated vertical velocity data assigned to upwellings, downwellings, and eddies. Thus, they cannot be used for interpretation of DVM modifications imposed by these major high-velocity events. Therefore, our analysis on impact of the major energetic events on DVM is entirely based on vertical redistribution of the acoustic backscatters.

Under-ice illumination was modelled using the exponential decay radiative transfer model (Grenfell and Maykut, 1977; Perovich, 1996). Figure 3c shows the sea-surface illuminance at mooring position computed for the open water conditions (no sea-ice and snow cover). Transmittance through the sea ice and snow cover to depth z in the ice was calculated using the following equation: $T(z)= i_0 e^{-K_t Z}$, where i_0 is the fraction of the wavelength-integrated incident irradiance transmitted through the top 0.1 m of the surface layer, and K_t is the total extinction coefficient in the snow or sea ice cover. The values adopted for the sea ice and snow covers were i_0=0.63, K_t=1.5, and i_0=50.9, K_t=0.1, respectively (Grenfell and Maykut, 1977). For computing under-ice illumination in Figures 3d and 3e, we use PIOMAS and HYCOM+CICE data on the simulated sea-ice thickness, respectively. The snow thickness on the top of the ice was taken from AMSR-E/Aqua observations. We accounted for the sea-ice and snow cover if the sea-ice concentration exceeds 90%. Cloud cover information was not utilized by this model taking due to high uncertainty of the cloud cover data (Liu and Key, 2016).

Time series of MVBS (Figures 7c-7g), vertical velocity component (Figures 8c-8g) and surface layer illumination (Figures 7b and 8b), computed for the HYCOM+CICE sea-ice thickness, are presented in a form of actograms showing a rhythm of activity. Variations during a day-long period are presented along the vertical axis of the actogram, while the long-term patterns of diurnal behavior can be assessed following the horizontal axis (e. g., Leise et al., 2013; Last et al., 2016; Hobbs et al., 2018). For the actograms of illuminance we introduced an artificial visual boundary on the illuminance colour scheme at 1 lux (gray to orange), the threshold, which corresponds to illuminance during the deep twilight.

Following Barber et al. (2015), we used the kinetic energy, $E = (U^2 + V^2) / 2$, derived from the zonal (U) and meridional (V) components of the current velocity to identify the major energetic events exceeding the two standard deviation threshold of ~ 500 $cm^2\ s^{-2}$. Using this threshold, Dmitrenko et al. (2018) identified thirteen major energetic events comprised of upwellings and downwellings. They are highlighted in Figures 7-9 with blue and pink shadings, respectively.

4 Sea-Ice and Oceanographic Settings

4.1 Sea-ice

The southern Beaufort Sea is seasonally ice-covered. It is dominated by the first-year pack ice with thickness gradually increasing from zero in September to ~80-90 cm in March-April (Melling et al., 2005). In the Canada Basin beyond the eastern Beaufort Sea continental slope, ice conditions are partly dominated by the multi-year pack ice with a mean thickness increasing from about 30 cm in August-September to 210-220 cm in May (Krishfield et al., 2014). The multi-year Greenland pack ice (>7 m thick) occupies the area to the north of the Canadian Arctic Archipelago and Greenland (e.g., Kwok et al., 2009).

The on-slope displacement of the multi-year pack ice from the Greenland and Ellesmere Island shelves was observed during winter 2005. This is evident from the sea-ice thickness ICESat data showing a west-

195 southward expansion of the Greenland pack in February - March 2005 (Figure 5d). This is in line with detecting multi-year ice on the RADARSAT satellite imagery acquired over the mooring position in May 2005 (Figure 6). The lighter areas in Figures 6c and 6d indicate the multi-year pack ice expanded over the mooring position before the sea-ice breakup in May 2005.

The satellite information on sea-ice thickness, however, is not consistent with PIOMAS. For February-
200 March 2004 and 2005, PIOMAS provides estimates of sea-ice thickness at mooring position of 1.87 m and 2.28 m, respectively (Figure 3b). In contrast, for the same time period, ICESat provides 1.5-1.4 m and 2.4-2.5 m, respectively (Figures 4c and 4d). This discrepancy is in line with the conclusions by Wang et al. (2016) that PIOMAS overestimates thicknesses for the thin ice area around the Beaufort Sea and underestimates the thick ice area around the northern Greenland and the Canadian Arctic Archipelago. For winter-spring 2003-04, PIOMAS
205 data agree relatively well with HYCOM+CICE data (Figure 3b). For January-May 2005, however, the discrepancy between PIOMAS and HYCOM+CICE increases from ~0.5 m on 1 January 2005 to ~1.3 m on 22 May 2005 (Figure 3b). During winter-spring 2005, spatial distribution of sea-ice thickness, derived from HYCOM+CICE simulations, shows the on-slope displacement of the multi-year pack ice from the Greenland and Ellesmere Island shelves (Figure 4), which is also revealed from the satellite observations (Figures 5 and 6a-6d). For winter-spring
210 2005, the HYCOM+CICE data on the multi-year pack ice >2 m thick over the mooring position are in line with detecting multi-year ice on the RADARSAT satellite imagery acquired before sea-ice breakup in May 2005 (Figure 6). Overall, the HYCOM+CICE simulations and satellite data suggest that during winter-spring 2005 sea-ice thickness over the mooring location exceeded that for 2004 by ~1 m with important implication for the under-ice illuminance values as evident from actograms of under-ice illuminance in Figures 3d and 3e. In what follows,
215 we use under-ice illuminance derived using the HYCOM+CICE simulations.

4.2 Temperature and salinity

The structure of the near-surface and intermediate water layers over the eastern Beaufort Sea upper continental slope, resolved by ADCP, is comprised of a mixture of river runoff and sea-ice meltwater and seawater of Pacific origin (Figure 2). A surface layer of relatively warm and low-salinity water (~27-29) is freshened by the
220 Mackenzie River runoff and sea-ice melt. Water with the salinity $29 < S < 33$ is generally assigned to Pacific Water (PW) – e.g., Dmitrenko et al. (2016). It is transported along the Beaufort Sea continental slope by an Alaskan branch of the PW flow emanating from Bering Strait. The relatively fresh PW layer impacts the halocline structure, producing a double halocline layer with a low stratified Upper Halocline water formed by the insertion of PW that overlies Lower Halocline water originating from the Eurasian Basin. In this study, we associated PW
225 with the broad temperature range between 1.5°C and –1.5°C approximately centered at $S \sim 32$ residing upper and low halocline layers (Figure 2). Pacific Summer Water (PSW) is broadly classified here as $T > –1.2$°C and $30 < S < 32$ (pink shading in Figure 2). In October 2003, July 2004, and September 2005, PSW occupied the upper intermediate water layer from ~25 to ~60 m depth (Figure 2). This water mass is usually comprised of the Chukchi Summer water transported through Herald Canyon on the western Chukchi shelf (Woodgate et al., 2005) and the
230 Alaskan Coastal water transported by the Alaskan coastal current through Barrow Canyon (Pickart et al., 2005). The underlying Pacific Winter Water (PWW) with the broad temperature minimum below –1.2°C centred at $S \sim 33$ (blue shading in Figure 2) is generated during freezing and brine rejection in the Bering and Chukchi Seas (Weingartner et al., 1998; Pickart, 2004). During 2003-2005, PWW occupied the lower intermediate water layer

in ~60-140 m depth (Figure 2). The warm and saltier Atlantic water with temperatures above 0°C and S > 33.5 underlies PWW at depths > 230 m that significantly exceeds the depth range resolved with ADCP measurements (Figure 2).

4.3 Water dynamics

The kinetic energy of currents over the eastern Beaufort Sea continental slope is mainly affected by the along-slope current component (Kulikov et al., 1998; Williams et al., 2006; Dmitrenko et al., 2016, 2018). For CA13, the maximum variability of currents is also consistent with along-slope direction, explaining ~ 70% of the total velocity variability (Dmitrenko et al., 2018). Thus, major energetic events highlighted in Figures 7-9 are primarily associated with along-slope flow dynamics, as also follows from the velocity time series in Figures 9c and 9d. Among thirteen major energetic events in Figures 7-9, four events were clearly attributed to the depth-intensified flow (#3D, 4D, 6D and 10D; pink shading in Figures 7-9) generated by ocean downwelling superimposed on the background bottom-intensified eastward shelfbreak flow. Six events are associated with the surface-intensified or barotropic flow (#1U, 2U, 7U, 8U, 9U, and 12U; blue shading in Figures 7-9). These events were attributed to ocean upwelling (Dmitrenko et al., 2018). While events #5U and 11U are depth-intensified, they are highlighted with blue shading because they are consistent with upwelling-favorable atmospheric forcing that usually drives the surface-intensified events. Vice versa, event #13D is surface-intensified, but it has been highlighted with pink shading because it is consistent with downwelling-favorable atmospheric forcing (Dmitrenko et al., 2018).

5 Diurnal Signal of the Mean Volume Backscatter Strength (MVBS) and Vertical Velocity

MVBS and vertical velocity actograms were computed for the depth of 28, 48, 68, 88 and 108 m (Figures 7c-7g and 8c-8g). These actograms reveal a rhythm of activity with diurnal cycle seen in the vertical axis of an actogram. The 2-year long variability of the diurnal cycle is observed along the horizontal axis.

5.1 Seasonal patterns

In general, MVBS actograms resemble seasonal variability of the diurnal signal following light conditions (Figures 7b-7g and 8b-8g). In the subsurface layer (28 m depth), a low MVBS corresponds to a relatively high illuminance during the day, while an elevated MVBS is consistent with a low illuminance during the night (Figures 7b and 7c). In contrast, at 108 m depth, MVBS shows an opposite pattern with a high MVBS during the light time of the day and a low MVBS in the darkness (Figures 7b and 7g). This variability in MVBS is consistent with DVM.

In general, the MVBS diurnal signal follows the seasonal variability of the sun illuminance during the entire year except for the period of the polar day when the diurnal pattern becomes significantly disrupted in the sub-surface water layer. Outside of the polar day, the diurnal changes in the sun illuminance are opposite to MVBS for the sub-surface layer, while at 108 m depth this relationship becomes positive. During the polar day, in the subsurface layer the MVBS diurnal rhythm vanishes (Figure 7c). In spring 2004, the vanishing of the MVBS diurnal pattern from the beginning of May corresponds to an increase of the midnight under-ice illuminance to >0.1 lux (Figures 7b and 7c). This modification lagged behind the sea-ice retreat off the mooring location by about one month (Figures 7a and 7c). In contrast, during spring 2005, significant deviation of the MVBS diurnal rhythm was delayed by about 3 weeks compared to 2004. The deviation of the MVBS diurnal pattern was recorded once

the sea-ice disappeared from the mooring location on 20 May 2005. Note that the satellite-derived data and HYCOM+CICE simulations for winter-spring 2005 show the sea-ice thickness over the mooring location exceeding that for 2004 by ~1 m (Figures 4-6). In spring 2005, the midnight under-ice illuminance >1 lux was lagging that in 2004 by about one week (Figure 7b).

For the PW layer, the behavior of the MVBS diurnal signal during the polar day is different from the sub-surface water layer. From about 1 April to 10 July 2004, the diurnal amplitude of MVBS signal was enhanced at the 68-108 m depth layer due to MVBS values lowered from ~ -61 to -66 dB during the astronomic midnight ±3 h (Figures 7e-7g). In contrast to the preceding and subsequent periods, no seasonal modulation of the MVBS diurnal cycle was observed at this time. This is in line with illuminance, showing almost no seasonal modulation during the midnight sun (Figure 7b). For the polar day period in 2005, however, enhancement of the MVBS diurnal signal seemed to be impacted by the short-term high MVBS events likely generated by intrusions of turbid water. These events were found to be most pronounced through the PSW layer where intrusions of turbid and relatively warmer water were observed during mooring recovery (Figures 2c, 7d, and 7e).

Following the midnight sun, the MVBS diurnal signal returned once the mooring position becomes 100% ice-covered since 7 November 2003 and 25 October 2004 (Figures 7a and 7c-7g). This is evident from enhancing the MVBS difference between the light (> 1 lux) and dark (< 1 lux) time for 28-48 m depth (Figure 7c-7d). The noticeable feature of the MVBS diurnal signal during civil twilight and the subsequent period until the end of April is a significant MVBS difference between 2003-2004 and 2004-2005 observed during the dark time through the entire water column resolved with ADCP observations (Figures 7c-7f). Another noticeable feature of MVBS during this period is numerous disruptions of the diurnal signal discussed below in sections 5.3.1 and 5.3.2.

Behind seasonality of diurnal signal in the MVBS time series, the seasonal cycling of the MVBS vertical distribution has been revealed (Figures 9a and 9b). For midnight, during low-light conditions from October to February (civil twilight length exceeds daylight length), MVBS tends to increase with depths from 28 to 108 m depth (Figure 8a). In March-June, the midnight MVBS shows an opposite tendency (Figure 9a). The MVBS midnight long-term mean, however, shows almost no difference from 28 to 108 m depth with a long-term mean of -0.6 dB. The seasonal cycle of the MVBS vertical distribution for the astronomic noon is different. From about winter to summer solstices, MVBS at 128 m depth exceeds that for 28 m depth by about 8 dB (Figure 9b). In contrast, during the ice-free period in June-August, the MVBS difference from 28 to 108 m depth tends to decrease down to about zero in late summer. The long-term mean for the astronomic noon (-5.3 dB, Figure 9b) shows a general tendency of MVBS to increase with depth.

The vertical velocity actograms also show a diurnal pattern around astronomic midnight (Figures 8c-8g) that is consistent with the MVBS diurnal rhythm in Figures 7d-7h. Net upward movement is regularly observed before the astronomic midnight once the under-ice dark-time illuminance was <0.1 lux (Figures 8b-8g). Moreover, the most intense upward flow was recorded during 1-3 h after the illuminance dropped below the 0.1 lux threshold. In contrast, a downward net flow was recorded following the tendency of under-ice illuminance to increase from midnight to noon once illuminance exceeds the 0.1 lux threshold (Figures 8b-8g). At the end of April 2004, once under-ice illuminance exceeded the 0.1 lux threshold for 24 h a day approaching the midnight sun, the vertical velocity diurnal signal completely vanished. During May-June 2004, however, a weaker net upward and downward diurnal movement of about ±0.5 cm s^{-1} was recorded at 68 and 88 m depth from noon to midnight (light blue to green shading in Figures 8e and 8f), and from midnight to noon (light green to yellow shading in

Figures 8e and 8f), respectively. This is consistent with the MVBS diurnal rhythm revealed through the PW layer during summer 2004 (Figures 7e-7g). Following the under-ice illuminance, well-pronounced velocity diurnal signal again appeared since end of August 2004 when the midnight under-ice illuminance decreases to the 0.1 lux threshold gradually returning to civil twilight. In spring 2005, the vertical velocity diurnal signal was relatively well pronounced until the midnight under-ice illuminance is below the 0.1 lux threshold (Figures 8b-8g). As of MVBS, complete cessation of a diurnal signal in vertical velocity in spring 2005 was observed at 68-88 m depth only when sea-ice started to retreat in mid-May (Figure 8a). In this case, complete cessation of diurnal signal lagged the 0.1 lux threshold by about 20 days (Figures 8b, 8e, and 8f). During the midnight sun 2005, the velocity diurnal rhythm is unrecognizable.

Finally, the velocity diurnal signal varies with depth. The upward and downward flow attributed to diurnal cycling is higher and less noisy at 68-88 m depth compared to the overlaying sub-surface layer at 28-48 m depth and to a lesser extent to the underlying water at 108 m depth (Figures 8c-8g).

5.2 Moon cycle

During the period of civil twilight when the sun is more than 6° below the horizon, the moonlight was the main source of illumination over the eastern Beaufort Sea continental slope (Figure 7b). The full moon succeeds with a mean period of 29.53059 days called a synodic or lunar month. During mid-winter (end of December), the full moon generates under-ice illuminance up to about 0.001 lux below the sea-ice layer with a thickness of around 1 m and ~20 cm snow depth over sea-ice (Figures 3b and 7b). In contrast, for the open water conditions, the full moon generates illuminance exceeding 0.1 lux (Figure 3c). Sea-ice strongly attenuates moonlight. Once sea-ice thickness exceeded ~2.5 m in April 2004 and February 2005, the moonlight transmittance through sea-ice is completely terminated (Figures 3b and 3e). While the cloud cover attenuates moon illumination, it was not considered for modelling under-ice illuminance due to high uncertainty of the cloud cover data (Liu and Key, 2016).

The MVBS diurnal signal is impacted by the moonlight, also attenuated by the cloud cover. Once the full moon (±6 days) occurred during the period of civil twilight, the cloud cover shows three low-cloud events with cloud cover ≤ 30% (#3, 4 in 2003-2004 and #3 in 2004-2005 in Figures 7a and 7b). During these events, the MVBS diurnal signal was significantly disrupted in the sub-surface layer, and a low MVBS was observed during the entire 24 h (Figures 7b and 7c). For the full moon event #4 in January 2004, during the astronomic midnight, a low MVBS at 28 m depth was associated with an elevated MVBS at 108 m depth, as evident from decreasing the MVBS difference from 28 to 108 m depth in Figure 9a. Overall, among 14 full moon events occurred in October-March 2003-2004 and 2004-2005 once the midnight under-ice illuminance was <1 lux, 3 events in February-March (#7 in 2004 and #6 and 7 in 2005) show complete cessation of the moonlight transmittance through sea-ice exceeding 2.5 m thick (Figure 7b). Events #1-5 in 2003-2004 and #1, 2, and 5 in 2004-2005 demonstrated similar anomalies of the MVBS difference from 28 to 108 m depth (Figure 9a). During the noon, however, this pattern is not obvious (Figure 9b).

Full moon event #1 in September-October 2004 gives an example of the moonlight impact on the MVBS diurnal signal (Figure 7). While the cloud cover during this event was relatively high (~50%, Figure 7a), the dark-time MVBS dropped by ~2 dB at 28 m depth, but elevated by ~4 dB at 68 and 88 m depth suggesting the downward displacement of the acoustic backscatters (Figures 7c and 7f-7g, respectively). At noon, however, MVBS elevated

by ~4 dB at 28 m depth (Figure 7c). Note that during this time the under-ice illuminance reduced as the mooring became ice-covered (Figure 7a). It is also important to point out that this full moon event partly overlays with upwelling #7U described below.

5.3 Short-term oceanographic events

The regular diurnal pattern of MVBS was disrupted during the short-term events lasting from several days to several weeks (Figures 7d-7h). These events also interplay with disruptions generated by moon cycling. We use actograms of vertical velocity to differentiate disruptions imposed by moonlight from those of dynamic origin (Figures 8c-8g). In general, the diurnal pattern remains well recognizable during the full moon events (Figures 8b-8g). In contrast, almost all significant or even complete short-term disruptions of the vertical velocity diurnal rhythm are related to upwelling or downwelling (Figures 8c-8g).

Dmitrenko et al. (2018) identified upwelling or downwelling events at CA13 using ADCP velocity data, the NCEP-derived wind and sea-level atmospheric data, sea surface height records at Tuktoyaktuk (Figure 1) and numerical simulations. All these events are highlighted in Figures 7-9 with blue and red shadings for upwelling and downwelling, respectively.

5.3.1 Upwelling Events

Upwelling events disrupt the MVBS diurnal signal in a similar way as the moonlight does. For upwelling #1U, MVBS at 108 m depth was elevated throughout the full 24 h period (Figure 7g). During the dark time (illuminance < 1 lux) at 28 m depth, MVBS reduced to the end of the event when the surface-intensified flow at 28 m depth shows maximum velocities exceeding 30 cm s^{-1} (Figure 9c). Moreover, upwelling #1U resulted in ~0.7°C temperature increase at 119 m depth (Figure 9f). Upwelling #2U, occurred right before the winter solstice, shows significant MVBS reduction at 28-48 m depth gradually vanishing to 108 m depth. Upwelling #5U occurred at the end of the ice-free season and shortly after the end of the midnight sun 2004. Therefore, the MVBS diurnal signal was relatively weak and noisy, especially at 28 m depth. However, MVBS increase at 88-108 m depth is likely attributed to upwelling. Upwelling #7U interplayed with full moon event #1 in September-October 2004. It seems that the first portion of this event until 3 October 2004 was dominated by the moonlight. Afterward, once the horizontal velocity at 28 m depth exceeded ~30 cm s^{-1} (Figure 9c), a slight reduction of MVBS is observed in 28-48 m depth during the dark time. In contrast to the preceding upwelling events, no elevated MVBS values were recorded in the overlying water layer. Upwelling #8U completely coincided with full moon event #2 in October-November 2004. As with the majority of the full moon and upwelling events, it shows the downward redistribution of the acoustic backscatters from 28-48 m to the deeper water layer (Figures 7c-7g, 9a, and 9b). A similar overlap between full moon and upwelling was observed during upwelling #9U. Significant MVBS reduction within 28-48 m was accompanied by elevated MVBS in 88-108 m depth during the latter part of this upwelling from 25 November to 5 December 2004. Overall, upwelling events #7-9 resulted in a gradual increase of temperature at 119 m depth from -1.55°C to -0.65°C (Figure 9f). Upwelling #11U shows an elevated MVBS during the light time at 88-108 m (Figures 7f, 7g, and 9b). However, no significant modifications of the MVBS diurnal signal were observed in the overlying water. The last upwelling #12U in May-June 2005 occurred during the midnight sun when the MVBS diurnal signal mostly vanished, and MVBS is noisy. We speculate that this noise is due to the enhanced concentration of suspended particles in the water column (Figure 2c).

Overall, among 8 upwelling events observed in 2003-2005, 6 events (#1, 2, 5, 7, 8, 9U) clearly show the MVBS reduction in the subsurface water layer at 28 m depth (Figure 7c). For upwellings #1, 5, 7, and 8U the midnight MVBS difference from 28 to 108 m depth tends to decrease, which is consistent with a downward redistribution of acoustic scatters (Figure 9a). This effect is similar to the MVBS response to the full moon events as described in section 5.2. It seems that the overlay between the upwelling and full moon can dominate the MVBS response to upwellings #7-9U (Figures 7b-7g). During the polar day, the MVBS diurnal signal is weak or completely disrupted, and its response to upwelling is barely traceable (upwelling #12, Figure 7b-7g). Finally, wind, forcing upwelling events, also impacts the sea-ice cover through the off-shelf displacement of the pack ice as evident for upwelling event #12 in May-June 2005 (Figure 7a).

5.3.2 Downwelling Events

Downwelling events disrupt the MVBS diurnal signal in the opposite way compared to upwellings and moonlight, moving acoustic backscatters upwards. Downwelling also interferes with MVBS modifications imposed by sea-ice and the MVBS diurnal signal deviations generated by moonlight. Wind, forcing downwelling events, also impacts the sea-ice cover through the on-shelf displacement of the pack ice as evident for downwelling events #4, 6 and 13D (Figure 7a). Deviations of the MVBS diurnal signal due to moon cycling interferes with those caused by downwelling event #3 complicating our analysis.

Downwelling #3D occurred at the end of 2003-2004 during civil twilight and strongly interfered with full moon event #4 (Figure 7). It seems that event #3D is entirely dominated by the moon, disrupting the MVBS diurnal signal as described in section 5.2. Downwelling #4D was recorded at the end of the polar day 2004 when the MVBS diurnal signal is terminated at 28-88 m depth (Figures 7c-7f). Wind, forcing downwelling #4D, displaced pack ice on-shelf, and the CA13 position was reoccupied by sea-ice for about 10 days with implication for under-ice illuminance. Figures 7c and 7d show that sea-ice and downwelling did not impact MVBS at 28-48 m depth. In contrast, the midnight sun diurnal signal at 68-88 m depth was disrupted due to elevating MVBS at 68-88 m depth during the dark-time (from 22 to 4 h, Figures 7e and 7f). At the same time, the midnight sun diurnal signal at 108 m depth remained undisturbed (Figure 7g). Downwelling #6D provides the most comprehensive example of how the MVBS diurnal signal is disrupted by downwelling. In contrast to the full moon and upwelling events, MVBS at 28-48 m depth was enhanced 24 h a day (Figures 7c and 7d) suggesting the upward redistribution of the acoustic backscatters from the underlying water layer (Figures 9a and 9b). Note that during this event water dynamics was dominated by along-slope depth-intensified flow increasing from ~5 cm s^{-1} at 28 m depth (Figure 9c) to >30 cm s^{-1} at 108 m depth (Figure 9d). Downwelling #10D was recorded at the end of civil twilight 2004-2005. It appears that the beginning of this event is impacted by the full moon (#4, 2004-2005) with the reduction of MVBS in the sub-surface layer at 28 m depth. However, by the end of downwelling #10D, once the bottom-intensified flow exceeded 100 cm s^{-1} at 128 m (Figure 9d), MVBS at 28-48 m depth tended to increase suggesting the upward redistribution of the acoustic backscatters, similar to downwelling #6D. Downwelling #13D occurred in mid-August 2005 following the midnight sun. During this time, the MVBS diurnal signal at 28 depth was not traceable. At 48-88 m depth, the midnight sun diurnal signal was likely masked due to the enhanced concentration of suspended particles in the water column (Figure 2c).

Overall, among 5 downwelling events recorded in 2003-2005, event #6D and partly #10D show disruption of the MVBS diurnal signal in the sub-surface water layer with MVBS elevated at 28-48 m depth in

response to downwelling. Downwelling events #4 and 13D occurred during and shortly after the midnight sun, respectively, when the sub-surface MVBS diurnal signal vanishes. Downwelling event #3D was dominated by the moonlight.

5.3.3 Eddies

Eddies are ubiquitous over the Arctic Ocean continental slope (e.g., Dmitrenko et al., 2008; Pnyushkov et al., 2018), and particularly over the Beaufort Sea continental slope (e.g., Spall et al., 2008; O'Brien et al., 2011). The eddy carrying entrained suspended particles was identified by Dmitrenko et al. (2018) based on the ADCP velocity and acoustic backscatter time series in February–March 2004 (Figures 7 and 10). One more eddy passed mooring position in December/January 2003/2004 right before downwelling #3D. In Figures 6-8 both eddies are highlighted with yellow shading.

The eddy in February–March 2004 provides an example of how the velocity field attributed to eddy passing disrupts the MVBS diurnal signal (Figure 10). The greatest tangential speed, exceeding 22 cm s^{-1}, marks the eddy core near 95 m depth (Figures 10a and 10b). Below the core at 119 m depth, a positive temperature anomaly of 0.25°C attributed to the eddy passing was recorded on 26 February 2004 (Figure 9f). The velocity signature of the eddy is hardly discernible shallower than about 50 m, where the temperature anomaly does not exceed ~0.1°C (Figures 9e, 10a, and 10b). During the dark time at 108 m depth (below the depth of the greatest tangential speed), an enhanced MVBS was observed between two maximal of the eddy tangential speed from 27 February to 2 March 2004 (Figure 10d). In contrast, during the daylight, a negative MVBS anomaly was recorded (Figures 7g and 10d). This completely inverted the MVBS diurnal signal observed at 108 m depth during the eddy passing. At 28-48 m depth, however, MVBS was not significantly modified. Nevertheless, MVBS was slightly elevated during the light time (Figures 7c, 7g and 10c). In contrast to water layers above and below the eddy core, from 26 February to 1 March the MVBS diurnal signal at 68-88 m depth was disrupted by the backscatter maximum recorded for 24 h a day (Figures 7e and 7f). It appears that this MVBS anomaly is attributed to the eddy-entrained suspended particles commonly recorded in this area (O'Brien et al., 2011).

The eddy in December/January 2003/2004 generated much less MVBS disturbance compared to the one in February–March 2004 (Figures 7c-7g). The core of the eddy was likely deeper than the ADCP transducer. A positive temperature anomaly at 119 m depth was 0.5°C (Figure 9f). A positive MVBS anomaly was recorded only at 108 m depth during 24 h a day (Figure 7g) likely indicating the eddy-entrained suspended particles. MVBS in the overlaying water layer was not significantly modified.

In summary, the eddy in February–March 2004 inverted the MVBS diurnal signal in the water layer below the eddy core defined by the greatest tangential speed of the horizontal flow. The eddy in December/January 2003/2004 generated no significant MVBS modifications as the eddy core was likely located below the ADCP.

6 Discussion

The two-year-long ADCP time series of MVBS and vertical velocity over the upper eastern Beaufort Sea continental slope are consistent with DVM of zooplankton. MVBS diurnal signal is generated by a diurnal movement of zooplankton toward the surface at dusk, and descent back the next morning before dawn. DVM demonstrates predator-avoidance behavior (Hays, 2003). Zooplankton keeps away from a relatively well-illuminated surface water layer during the light time reducing the light-dependent mortality risk. The acoustic data

from the single-frequency ADCP do not provide any information on the identity of organisms responsible for the observed DVM patterns, and proper studies on DVM have not been carried out in the Beaufort Sea prior to the present work. Thus, our analysis is significantly limited by deficiency of zooplankton observations. Moreover, a comprehensive analysis of the scattering species comprising DVM is logistically impossible for the long-term deployments in the seasonally ice-covered and remote areas in the high Arctic. This prohibits identification of specific species whose DVM was detected by the 300 kHz ADCP and altered by the different environmental factors including illuminance and water dynamics. The deficiency of our analysis clearly defines a necessity for expanding mooring observations using underwater electronic holographic cameras such as those described by Sun et al. (2007).

In general, DVM at CA13 is controlled by light conditions (Figures 7 and 8). As for the other areas of the ocean, DVM is triggered by local solar variations, and the timing of migration is sensitive to changes in seasonal day length (e.g., van Haren and Compton, 2013). Our results show that DVM responds to (i) seasonality of the sunlight, (ii) seasonality of sea-ice cover that attenuates light transmission to the water column, and to a lesser extent to (iii) moonlight. Moreover, (iv) DVM can be modified or completely disrupted during highly energetic current events generated by upwelling, downwelling or eddy passing. Our results also suggest that the interplay between all these factors impacts DVM at CA13. Furthermore, MVBS is not entirely controlled by DVM. The suspended particles in the water column enhance acoustic scattering, impacting DVM during the midnight sun (Figures 2a, and 7b, 7d, and 7e), and also attenuating light intensity in the water column. Below we discuss all these factors and their impact on DVM in more detail.

6.1 DVM seasonal cycle, sea-ice cover, and suspended particles

It appears that DVM is triggered once the estimated near-surface illuminance falls below the 0.1-lux threshold (Figures 7 and 8). This suggests that the diurnal movement of zooplankton toward the surface at dusk starts once the near-surface illuminance decreased to ~0.1 lux, and descends back the next morning before dawn as soon as the near-surface illuminance exceeds 0.1 lux. DVM follows changes in seasonal day length, and it stops at the sub-surface layer as soon as near-surface illuminance retains above ~0.1 lux for 24 h a day (Figures 7b-7g). At the CA13 latitude (71°21.356'N), the estimated value of near-surface or under-ice illuminance exceeds the 0.1 lux threshold for about 55 and 50 days before the midnight sun in 2004 and 2005, respectively (Figure 7b). During fall 2004, the sub-surface DVM returned about 27 days after the polar day season, once the midnight near-surface illuminance dropped below ~0.1 lux threshold around 28 August (Figures 6b-6g). Our results on the light threshold are consistent with the preferendum (isolume) hypothesis (e.g., Cohen and Forward, 2009). A variant of the preferendum hypothesis, the absolute intensity threshold hypothesis, suggests that an ascent at sunset is initiated once the light intensity decreases below a particular threshold level and a descent at sunrise occurs when the light intensity increases above the threshold intensity (e.g., Cohen and Forward, 2019). This is in line with our findings on an absolute 0.1-lux threshold of light, which corresponds to the moonlight illuminance at the gibbous moon during clear sky (Gaston et al., 2014).

The inter-annual variability in estimated under-ice illuminance is entirely attributed to the sea-ice thickness. During the ice season, the mean cloud cover (~40%) showed insignificant interannual variability (Figure 7a); thus, the cloud cover was not taken into account. Our results reveal that sea-ice cover modifies the DVM seasonal cycle by attenuating under-ice illuminance. During winter-spring 2004, CA13 was primarily

covered with the first-year pack ice of about 1.6 m thick (Figures 3b, 4 top, 5a, and 5b). In contrast, during the same time in 2005, the eastern Beaufort Sea continental slope was occupied by the multi-year pack ice of about 2.6 m thick (Figures 3b, 4 bottom, 5c, and 5d). We suggest that this increased sea-ice thickness extended the DVM seasonal cycle toward the polar day of 2005. In May 2005, the 0.1-lux threshold estimated for ~2.5 m thick ice lags that for 2004 by about 5 days (Figure 7b). Following ice-diminished illuminance in April-May 2005, DVM at 28 m depth was recorded until the beginning of May 2005. Moreover, DVM maintained integrity at 68-108 m depth until the open-water season started in mid-May 2005 (Figures 7c and 7e-7g, respectively). In contrast, during spring 2004, DVM vanished about 12 and 28 days ahead of the polar day and open-water season, respectively (Figures 7). We suggest that this inter-annual DVM variability is consistent with under-ice illuminance. Its estimated value for mid-May 2004 (≥10 lux) exceeds that for May 2005 by a factor of 10 (Figure 7b).

The MVBS actograms show asymmetry of the DVM seasonal cycle to the summer solstice (Figures 7b-7g). In summer 2004, the DVM seasonal cycle terminated about 54 days before the summer solstice but resumed, lagging summer solstice by 67 days. This asymmetry, being consistent with the estimated 0.1-lux threshold, is likely attributed to the seasonal sea-ice cover. During spring, the polar day begins when the eastern Beaufort Sea continental slope is still ice-covered (Figures 6a and 6b), which governs attenuation of light below the ice. In contrast, after the polar day is ended, the eastern Beaufort Sea continental slope remains ice-free or partly ice-covered until the end of October allowing sunlight to illuminate the near-surface water layer.

In the subsequent winters, the DVM backscatter intensity shows significant interannual variability. The dark-time MVBS during winter 2003-2004 exceeds that for winter 2004-2005 by ~ 3-5 dB (Figures 7c-7g). We attribute this inter-annual variability to attenuation of light by a thicker ice cover in winter 2004-2005, as follows from our preceding discussion. Satellite data and model simulations show that the eastern Beaufort Sea continental slope was occupied by Greenland pack ice during winter-spring 2005 (Figures 4-6) that results in the reduced estimate of under-ice illuminance by a factor of 10 (Figure 7b). For example, during full moon events #6 and 7 in February-March 2005, the night-time moonlight illuminance felt down to the background night-time illuminance <0.0001 lux (Figure 7b).

In general, our results on the sea-ice impact on DVM show that DVM is well synchronized with the light/dark cycle modified by the sea-ice cover shading. It appears that thicker ice observed during winter 2004-2005 reduced the backscatter values (Figures 7c-7g), which likely demonstrates a light-mediated response of the zooplankton involved in DVM. This is in line with Berge et al. (2009) reporting a stronger polar night DVM in the ice-free Svalbard fjord compared to the ice-covered fjord. Vestheim et al. (2014) reported on shallowing DVM in Oslofjord in response to the freeze-up and subsequent snowfalls. They attributed this shallowing to a relative reduction of light intensities, which is similar to that observed over the eastern Beaufort Sea continental slope during winter-spring 2005. La et al. (2015) suggested that sea-ice diminishes DVM signals by blocking the detectable light intensity for DVM with depth during the Antarctic winter. At the same time, our results contrast with the observations of Wallace et al. (2010). They found no difference in time of the DVM onset and cessation between the seasonally ice-covered and ice-free Svalbard fjords, insisting on the role of the relative change in irradiance for triggering DVM. This discrepancy highlights an important difference between sea-ice in the Svalbard fjords and the eastern Beaufort Sea continental slope. Rijpfjorden in Svalbard is seasonally ice-covered with land-fast ice of ~0.8 m thick (Wallace et al., 2010). In contrast, in spring 2015 the eastern Beaufort Sea

continental slope was occupied by 2.6 m thick multi-year Greenland pack ice (Figures 3b, and 4-6) favoring the synchronized DVM to extend toward the midnight sun.

Our data show that, during the midnight sun 2004, DVM ceased only at 28 m depth. In the underlying PW layer at 48-108 m depth, DVM continued until the beginning of July 2004 (Figures 7c-7e). However, DVM in the PW layer did not occur in phase with the 24-h light cycle. It seems that zooplankton was conducting regular synchronized DVM, but it was still avoiding relatively well-illuminated sub-surface water. This is in line with a predator-avoidance behavior during transitional seasons, but without seasonal modulation, because the sun is above the horizon 24 h a day. In fact, zooplankton limits DVM to the PSW water layer with relatively high chlorophyll fluorescence values during late summer (Figure 2). This can indicate high concentrations of phytoplankton (e.g., La et al., 2018), which zooplankton feeds on. The availability of phytoplankton can be an important factor triggering seasonal variability in DVM (e.g., La et al., 2015).

Usually, synchronized DVM stops during the midnight sun, consistent with a predator-avoidance behaviour of zooplankton conducting DVM (e.g., Blachowiak-Samolyk et al., 2006; Cottier et al., 2006; Wang et al., 2015; Darnis et al., 2017). However, Fortier et al. (2001) reported a clear midnight sun DVM in copepods under the spring ice of Barrow Strait at the centre of the Canadian Arctic Archipelago. They argued that absolute light intensity below sea ice decreases to the thresholds at which the feeding activity of fish slows down. Moreover, DVM below 2-m thick ice in the Canada Basin during the midnight sun was recently reported by La et al. (2018). Following Fortier et al. (2001), we speculate that the absolute light intensity through the PW layer at CA13 was below the threshold of predators' perception allowing DVM during the midnight sun 2004. However, the midnight sun DVM was not obvious in 2005.

We suggest that the midnight sun DVM in 2005 was likely impacted by the enhanced concentration of suspended particles through the PSW layer. Suspended particles return the ADCP acoustic signal, producing enhanced MVBS 24 h a day. For example, Petrusevich et al. (2020) reported on enhanced MVBS in Hudson Bay recorded by 300 kHz RDI Workhorse ADCP. They attributed this signal to the suspended particles released to the water column during ice melt. In contrast to the vertically synchronized DVM, suspended particles generated noise that can mask DVM during the midnight sun 2005 as evident from Figures 7d-7f. On the CTD profile taken in September 2005, high particulate beam attenuation layers around 25 and 50 m depth match temperature maxima up to 1.3°C (Figure 2c). Moored CTD at 49 m depth shows several maxima up to 0.5°C following summer solstice 2005 (Figure 9e). Two temperature maxima in the beginning and mid-June 2005 (Figure 9e) match MVBS maxima at 68-88 m depth (Figure 7f and 7g). This suggests that MVBS maxima in actograms are generated by lateral advection of warm and turbid water layers. The formation of this water is likely attributed to wind-forced vertical mixing over the Beaufort Sea shelf involving surface riverine water heated by solar radiation and enriched with suspended particles. Alternatively, suspended particles can be attributed to resuspension of bottom sediments over the Beaufort Sea shelf. In any case, regardless of the source of suspended particles, their enhanced concentration in the water column during summer 2005 resulted in increased light attenuation (e.g., Hanelt et al., 2001), which potentially modified DVM during the midnight sun 2005.

6.2 DVM modifications by moonlight

In general, interpretation of the DVM modifications due to the moonlight is not straightforward. The dark-time MVBS in Figure 7c shows cumulative effect of sea-ice, cloud cover, water dynamics and moonlight. Individual

events are often overlaid, and uncertainty in cloud cover also introduces an additional complication. Furthermore, during February-March, the moonlight below sea-ice is strongly attenuated (2004) or completely absorbed by sea-ice (2005) - Figure 3e. Moreover, under-ice vertical velocity data does not show DVM disruptions during full moon phases (Figure 8). However, MVBS actograms in Figures 7c-7g indicate modifications of DVM during a few days near the time of the full moon. These modifications are consistent with a lack of the upward moving zooplankton during the dark-time. They were observed from October to March including the civil twilight (Figures 7b-7g). The most pronounced moonlight modifications were observed during low cloud cover periods (Figure 7).

While our results on the moon's modifications of DVM are not entirely conclusive, they are consistent with those previously reported for the Arctic and sub-Arctic regions. Moonlight plays a central role in structuring predator-prey interactions in the Arctic during the polar night below the ice (Last et al., 2016). It has been shown that during the polar night the moon's influence on DVM in the Arctic results in the zooplankton downward migration to deeper water for a few days near the time of the full moon (Webster et al., 2015; Last et al., 2016). This is consistent with a concept that the moon phase cycle in the zooplankton migration is a global phenomenon in the ocean as suggested by Gliwicz (1986). As to DVM, the reason for the moon's modification was hypothesized to be a predator-avoidance behaviour against predators capable of utilizing the lunar illumination. Note, however, that during civil twilight 2005 below ~1.8 m thick pack ice, zooplankton responded to the estimated lunar illumination of 0.001 lux (Figures 7b and 7c), which is far below the threshold of human and predators' perception. The moon's modification of DVM during the 2005 civil twilight suggests that zooplankton shows extraordinary sensitivity to illuminance (Båtnes et al., 2013; Cohen et al., 2015; Last et al., 2016; Petrusevich et al., 2016).

6.3 DVM disruptions related to water dynamics

Our results revealed that water dynamics temporally impact DVM by disrupting the diurnal rhythm. Upwelling affects DVM the same way as moonlight forcing zooplankton to avoid the sub-surface water layer during the dark time of the day. In contrast, downwelling seems to force zooplankton to stay in the upper intermediate water layer (consisted of PSW) for 24 h a day. During downwelling, zooplankton likely avoids the lower intermediate layer comprised by PWW. The eddy disrupts DVM in the water layer below the eddy core inverting the MVBS diurnal signal. It seems that zooplankton prevents crossing the water layer occupied by the eddy core. The general impression is that zooplankton likely avoids enhanced water dynamics.

The characteristic feature of high-energetic events recorded at CA13 is the depth-dependent behavior of the horizontal flow. For upwelling and downwelling over the eastern Beaufort Sea continental slope, this feature is generated by the superposition of the background and wind-forced flow (Dmitrenko et al., 2018). The wind-driven barotropic flow generated by upwelling and downwelling wind forcing is superimposed on the background bottom-intensified shelfbreak current depicted by a dashed line in Figure 11c (Dmitrenko et al., 2018). For the downwelling storms, this effect amplifies the depth-intensified background circulation with enhanced PWW transport towards the Canadian Arctic Archipelago (Figure 11b and 11c, right). For the upwelling storms, the shelfbreak current is reversed, which results in surface-intensified flow moving in the opposite direction (Dmitrenko et al., 2018 and Figures 11a and 11c, left). The baroclinic eddies over the Beaufort Sea continental slope are likely explained by the shelfbreak current baroclinic instability (Spall et al., 2008).

It appears that upwelling, downwelling, and eddies disrupt DVM by generating a water layer with an enhanced gradient of horizontal velocity. We suggest that zooplankton avoids crossing this interface during diurnal migration, disrupting DVM. For crossing the high-gradient velocity layers, zooplankton has to spend additional energy. However, zooplankton is known for demonstrating a strategy of minimizing energy use while crossing water layers with enhanced water dynamics (Eiane et al., 1998; Basedow et al., 2004; Marcus and Scheef, 2009; Petrusevich et al., 2016, 2020; Cohen and Forward, 2019). For example, Petrusevich et al. (2016) reported on the DVM deviation in an ice-covered Northeast Greenland fjord in response to the estuarine-like circulation generated by a polynya opening over the fjord mouth (Dmitrenko et al., 2015). Overall, we suggest that in addition to the predator and starvation avoidance, the zooplankton beware to cross the high-gradient velocity layers remaining behind or below them, hence disrupting DVM.

It is suggested that upwelling and downwelling disrupt DVM. Zooplankton is transported offshore during upwelling and shoreward during downwelling (for review see Queiroga et al., 2007). For upwelling, the wind-driven Ekman offshore transport leads to offshore dispersal and wastage from coastal habitats. This is consistent with MVBS reduction recorded in the sub-surface layer during upwelling events (Figure 7c). In fact, zooplankton can adjust migration strategy to avoid off-shore transport, reversing DVM (Poulin et al., 2002a,b). Moreover, zooplankton can avoid sweeping off-shore by upwelling and onshore by downwelling, maintaining preferred depth in the face of converging and downwelling flow (Shanks and Brink, 2005). DVM can be also impacted by the property of upwelled water. Huiwu et al. (2015) reported that DVM deviation is caused by aggregation of zooplankton in the upper 10-m layer in response to upwelling over the Chukchi Sea shelf northwest of the Alaskan coast. They explained DVM deviation by the nutrient-rich upwelled water, which favors an enhanced light attenuation by heavy phytoplankton. This, in turn, allows zooplankton to spend most of its time at the near-surface water layer.

We speculate that DVM disruptions attributed to upwelling and downwelling are primarily dominated by along-slope transport rather than the cross-slope transport. In addition to enhancing the cross-slope transport, upwelling and downwelling over the Beaufort Sea continental slope strongly modify along-slope transport through generating depth-dependent currents over the continental slope (Figure 11; Dmitrenko et al., 2016, 2018). We suggest that zooplankton avoids crossing horizontal velocity interface, generated by the superposition of wind-driven circulation and along-slope jet. This strategy is evident from the DVM disruption caused by the baroclinic eddy in February-March 2004. Below the depth of the maximum tangential speed (~90 m), DVM was found to be reversed (Figures 6g and 9). This is consistent with reversing DVM to avoid the upwelling induced off-shore Ekman transport in the Peru-Chile upwelling system (Poulin et al. 2002a,b). The reversed DVM in response to eddy passing clearly shows that zooplankton is capable to adjust its strategy of diurnal migration to avoid enhanced water dynamics.

7 Conclusions

Based on the 2-year long time series from the mooring deployed over the upper eastern Beaufort Sea continental slope from October 2003 to September 2005, we conclude that the acoustic backscatter is dominated by DVM. DVM is controlled by the following different external forcings that also interplay.

(i) *Illuminance*. It is, in turn, controlled by the solar and moonlight cycling and sea-ice cover. The solar cycle controls DVM and its seasonal variability. In addition, sea-ice modifies seasonal patterns of DVM through light

attenuation. A thicker multi-year Greenland pack ice present in winter-spring 2005 reduced the number of acoustic backscatters in the water column compared to that of winter-spring 2004 when the first-year pack ice dominated. Meanwhile, during spring 2005, the multi-year Greenland pack ice favored DVM prolongation toward the midnight sun due to the sea-ice shading the under-ice water layer. During civil twilight, the moon cycle generally modifies DVM, but this modification also depends on the sea-ice thickness and cloud cover. The strongest deviation was observed during mid-fall to early winter when sea ice is absent or relatively thin, and the NCEP-derived cloud cover is <30%. These deviations are associated with significant night-time reduction of acoustic backscatters in the sub-surface layer. It seems that the full moon stimulates zooplankton to avoid the sub-surface layer.

(ii) *Water dynamics*. Upwelling and downwelling disrupt DVM. We found that this disruption is dominated by the along-slope water dynamics rather than the cross-slope Ekman transport. The surface-intensified along-slope flow generated by upwelling drives zooplankton to the lower intermediate depths hosting PWW to avoid the sub-surface layer. Zooplankton similarly respond to upwelling as it does to the moonlight. Thus, DVM disruptions induced by upwelling often interferes with the one generated by moonlight. In contrast, the bottom-intensified along-slope flow generated by downwelling modifies DVM through accumulating zooplankton in the upper intermediate layer occupied by PSW. The baroclinic eddy reverses DVM below the eddy core. We suggest that the zooplankton's response to upwelling, downwelling, and eddy is consistent with adjusting DVM to avoid enhanced water dynamics.

In contrast to many previous studies of the high-Arctic regions, at ~71°N latitude we recorded DVM during the midnight sun. During the ice-free season of the midnight sun 2004, DVM was observed through the PW layer. This DVM is likely limited by the depth of chlorophyll maxima in PSW. In 2005 the midnight sun DVM seemed to be masked by a high acoustic scattering level attributed to warmer and turbid layers observed through PSW.

Our analysis was limited by deficient zooplankton observations. A comprehensive analysis of the scattering species comprising DVM is logistically impossible for the long-term deployments in the seasonally ice-covered and remote areas in the high Arctic. This prohibits identification of specific species whose DVM was detected by the 300 kHz ADCP and altered by the different environmental factors including illuminance and water dynamics.

Acknowledgments

We appreciate Jørgen Berge from the Arctic University of Norway and another anonymous reviewer for their constrictive comments and suggestions. The data used for this research were collected under the ArcticNet framework, project Long-Term Oceanic Observatories in the Canadian Arctic. We gratefully acknowledge the support by the Canada Excellence Research Chair (CERC) and the Canada Research Chairs (CRC) programs. This work is a contribution to the joint Canadian-Danish-Greenland Arctic Science Partnership, Québec-Ocean, and the Canada Research Chair on the response of Arctic marine ecosystems to climate warming. The research was also partly supported by the National Sciences and Engineering Research Council of Canada (IAD: grant RGPIN-2014-03606, JKE: grant RGPIN/435373-2013).

Data

The ADCP data are available through the Polar Data Catalogue at https://www.polardata.ca/pdcsearch/, CCIN Reference #11653 (Gratton et al., unpublished).

Authors' contributions

Contributed to conception and design: IAD, VP, GD, SR, DB
Contributed to acquisition of data: JKE, AK, GD, AF, LF
Contributed to analysis and interpretation of data: IAD, VP, AK, GD, SK
Drafted and/or revised the article: IAD, VP, AK, GD, SR
Approved the submitted version for publication: IAD

References

Barber, D.G, Hop, H., Mundy, C.J., Else, B., Dmitrenko, I.A., Tremblay, J.-E., Ehn, J.K., Assmy, P., Daase, M., Candlish, L.M., and Rysgaard, S.: Selected physical, biological and biogeochemical implications of a rapidly changing Arctic Marginal Ice Zone, Prog. Oceanogr., 139, 122–150, doi:10.1016/j.pocean.2015.09.003, 2015.

Basedow, S., Eiane, K., Tverberg, V. and Spindler, M.: Advection of the zooplankton in an Arctic fjord (Kongsfjorden, Svalbard), Estuarine Coastal Shelf Sci., 60(1), 113–124, doi:10.1016/j.ecss.2003.12.004, 2004.

Båtnes, A. S., Miljeteig, C., Berge, J., Greenacre, M., and Johnsen, G.: Quantifying the light sensitivity of Calanus spp. during the polar night: potential for orchestrated migrations conducted by ambient light from the sun, moon, or aurora borealis?, Polar Biol., 1, 15, doi: 10.1007/s00300-013-1415-4, 2013.

Berge, J., Renaud, P.E., Darnis, G., Cottier, F., Last, K., Gabrielsen, T.M., Johnsen, G., Seuthe, L., Weslawski, J.M., Leuc, E., Moline, M., Nahrgang, J., Søreide, J.E., Varpeb, Ø., Lønne, O.J., Daasea, M., and Falk-Petersen, S.: In the dark: A review of ecosystem processes during the Arctic polar night, Prog. Oceanogr., 139, 258–271, doi:10.1016/j.pocean.2015.08.005, 2015.

Berge J., Cottier, F., Last, K.S., Varpe, Ø., Leu, E., Søreide, J., Eiane, K., Falk-Petersen, S., Willis, K., Nygård, H., Vogedes, D., Griffiths, C., Johnsen, G., Lorentzen, D., and Brierley, A.S., Diel vertical migration of Arctic the zooplankton during the polar night, Biol. Lett., 5, 69–72, doi: 10.1098/rsbl.2008.0484, 2009.

Brierley, A.S., Brandon, M.A., and Watkins, J.L., An assessment of the utility of an acoustic Doppler current profiler for biomass estimation, Deep Sea Res. Part I, 45(9), 1555–1573, doi: 10.1016/S0967-0637(98)00012-0, 1998.

Brierley, A.S., Diel vertical migration, Curr. Biol., 24, R1074−R1076, doi: 10.1016/j.cub.2014.08.054, 2014.

Chassignet, E.P., Hurlburt, H.E., Smedstad, O.M., Halliwel, G.R., Hogan, P.J., Wallcraft, A.J., Baraille, R., and Bleck, R., The HYCOM (Hybrid Coordinate Ocean Model) data assimilative system, Journal of Marine Systems, 65, 60–83, doi: 10.1016/j.jmarsys.2005.09.016, 2007.

Cohen, J.H., Berge, J., Moline, M.A., Sørensen, A.J., Last, K., Falk-Petersen, S., Renaud, P.E., Leu, E.S., Grenvald, J., Cottier, F., Cronin, H., Menze, S., Norgren, P., Varpe, Ø., Daase, M., Darnis, G., and Johnsen, G., Is Ambient Light during the High Arctic Polar Night Sufficient to Act as a Visual Cue for Zooplankton?, PLoS ONE, 10(6), e0126247, doi: 10.1371/journal.pone.0126247, 2015.

Cavalieri, D.J., Markus, T., and Comiso, J.C., AMSR-E/Aqua Daily L3 12.5 km Brightness Temperature, Sea Ice Concentration, & Snow Depth Polar Grids, Version 3. Boulder, Colorado USA. NASA National Snow and Ice Data Center Distributed Active Archive Center, doi: 10.5067/AMSR-E/AE_SI12.003, 2014.

Cohen, J.H., and Forward, R.B., Zooplankton Diel Vertical Migration - A Review Of Proximate Control, Oceanography and marine biology: An Annual Review, 47, 77-109, 2009.

Cohen, J.H., and Forward, R.B., Vertical Migration of Aquatic Animals, Encyclopedia of Animal Behavior (Second Edition), Elsevier, 546-552, doi: 10.1016/B978-0-12-809633-8.01257-7, 2019.

Cottier F.R., Tarling, G.A., Wold, A., and Falk-Petersen, S., Unsynchronised and synchronised vertical migration of the zooplankton in a high Arctic fjord, Limnol. Oceanogr., 51, 2586–2599, doi: 10.4319/lo.2006.51.6.2586, 2006.

Darnis, G., Hobbs, L., Geoffroy, M., Grenvald, J.C., Renaud, P.E., Berge, J., Cottier, F., Kristiansen, S., Daase, M., Søreide, J.E., Wold, A., Morata, N., and Gabrielsen, T., From polar night to midnight sun: Diel vertical migration, metabolismand biogeochemical role of the zooplankton in a high Arctic fjord (Kongsfjorden, Svalbard), Limnol. Oceanogr., 62, 1586–1605, doi: 10.1002/lno.10519, 2017.

Deines, K.L., Backscatter estimation using Broadband acoustic Doppler current profilers, in Proceedings of the IEEE Sixth Working Conference on Current Measurement (Cat. No.99CH36331), pp. 249–253, IEEE, San Diego, Calif, 1999.

Dmitrenko, I.A., Kirillov, S.A., Myers, P.G., Forest, A., Tremblay, B., Lukovich, J.V., Gratton, Y., Rysgaard, S., and Barber, D.G., Wind-forced depth-dependent currents over the eastern Beaufort Sea continental slope: Implications for Pacific water transport, Elem. Sci. Anth., 6, 66, doi: 10.1525/elementa.321, 2018.

Dmitrenko, I.A., Kirillov, S.A., Forest, A., Gratton, Y., Volkov, D.L., Williams, W.J., Lukovich, J.V., Belanger, C., and Barber, D.G., Shelfbreak current over the Canadian Beaufort Sea continental slope: Wind-driven events in January 2005, J. Geophys. Res., 121(4), 2447-2468, doi: 10.1002/2015JC011514, 2016.

Dmitrenko, I.A., Kirillov, S.A., Rysgaard, S., Barber, D.G., Babb, D.G., Pedersen, L.T., Koldunov, N.V., Boone, W., Crabeck, O., and Mortensen, J., Polynya impacts on water properties in a Northeast Greenland Fiord, Estuarine Coastal Shelf Sci., 153, 10–17, doi:10.1016/j.ecss.2014.11.027, 2015,

Dmitrenko, I.A., Wegner, C., Kassens, H., Kirillov, S.A., Krumpen, T., Heinemann, G., Helbig, A., Schröder, D., Hölemann, J.A., Klagge, T., Tyshko, K.P., and Busche, T., Observations of supercooling and frazil ice formation in the Laptev Sea coastal polynya, J. Geophys. Res., 115, C05015, doi: 10.1029/2009JC005798, 2010.

Dmitrenko, I.A., Kirillov, S.A., Ivanov, V.V., and Woodgate, R.A., Mesoscale Atlantic water eddy off the Laptev Sea continental slope carries the signature of upstream interaction, J. Geophys. Res., 113, C07005, doi: 10.1029/2007JC004491, 2008.

Eiane, K., Aksnes, D., and Ohman, M., Advection and the zooplankton fitness, SARSIA, 83, 87–93, doi: 10.1080/00364827.1998.10413674, 1998.

Falk-Petersen, S., Leu, E., Berge, J., Kwasniewski, S., Nygårdb, H., Røstad, A., Keskinen, E., Thormar, J., Quillfeldt, C., Wold, A., and Gulliksen, B., Vertical migration in high Arctic waters during autumn 2004, Deep Sea Res., Part II, 55(20-21), 2275–2284, doi: 10.1016/j.dsr2.2008.05.010, 2008.

Fielding, S., Griffiths, G., and Roe, H.S.J., The biological validation of ADCP acoustic backscatter through direct comparison with net samples and model predictions based on acoustic-scattering models, ICES J. Mar. Sci. J. du Cons., 61(2), 184–200, doi: 10.1016/j.icesjms.2003.10.011, 2004.

Fortier, M, Fortier, L., Hattori, H., Saito, H., and Legendre, L., Visual predators and the diel vertical migration of cope-pods under Arctic sea ice during the midnight sun, J. Plankton Res., 23, 1263–1278, doi: 10.1093/plankt/23.11.1263, 2001.

Gaston, K.J., Duffy, J.P., Gaston, S., Bennie, J., and Davies, T.W., Human alteration of natural light cycles: causes and ecological consequences, Oecologia, 176, 917–931, doi: 10.1007/s00442-014-3088-2, 2014.

Gliwicz, Z.M., A Lunar Cycle in The Zooplankton, Ecology, 67(4), 883-897, doi: 10.2307/1939811, 1986.

Gratton, Y, Ingram, G., Carmack, E., Van Hardengerget, B., Forest, A., Fortier, L., Blondeau, S., Massot, P., and Michaud, L., Long-term oceanic observatories (moorings) in the Beaufort Sea during the Canadian Arctic Shelf Exchange Study, 2002–2004, doi: 10.5884/11653, unpublished.

Grenfell, C.G., and Maykut, G.A., The optical properties of ice and snow in the Arctic Basin, J. Glaciol., 18(80), 445–463, doi: 10.3189/S0022143000021122, 1977.

Grenvald, J.C., Callesen, T.A., Daase, M., Hobbs, L., Darnis, G., Renaud, P.E., Cottier, F., Nielsen, T.G., and Berge, J., Plankton community composition and vertical migration during polar night in Kongsfjorden, Polar Biology, 39, 1879–1895, doi: 10.1007/s00300-016-2015-x, 2016.

Hanelt, D., Tüg, H., Bischof, K., Groß, C., Lippert, H., Sawall, T., and Wiencke, C., Light regime in an Arctic fjord: a study related to stratospheric ozone depletion as a basis for determination of UV effects on algal growth, Marine Biology, 138(3), 649–658, doi: 10.1007/s002270000481, 2001.

Hays G.C., A review of the adaptive significance and ecosystem consequences of the zooplankton diel vertical migrations, Hydrobiologia, 503, 163–170, doi: 10.1023/B:HYDR.0000008476.23617.b0, 2003.

Hobbs, L., Cottier, F.R., Last, K.S., and Berge, J., Pan-Arctic diel vertical migration during the polar night, Mar. Ecol. Prog. Ser., 605, 61– 72, doi: 10.3354/meps12753, 2018.

Hunke, E.C., Viscous-plastic sea ice dynamics with the EVP model: linearization issues, Computational Physics, 170, 18–38, doi: 10.1006/jcph.2001.6710, 2001.

Kalnay, E., et al., The NCEP/NCAR 40-year reanalysis project, Bull. Am. Meteorol. Soc., 77, 437–471, doi: 10.1175/1520-0477(1996)077<0437:TNYRP>2.0.CO;2, 1996.

Kirillov, S, Dmitrenko, I., Tremblay, B., Gratton, Y., Barber, D., and Rysgaard, S., Upwelling of Atlantic Water along the Canadian Beaufort Sea continental slope: Favorable atmospheric conditions and seasonal and interannual variations, J. Climate, 29(12), 4509–4523, doi: 10.1175/JCLI-D-15-0804.1, 2016.

Kosobokova, K.N., Diurnal vertical distribution of Calanus Hyperboreus Kroyer and Calanus Glacialis Jaschnov in Central Polar Basin, Okeanologiya, 18(4), 722–728, 1978.

Krishfield, R.A., Proshutinsky, A., Tateyama, K., Williams, W.J., Carmack, E.C., McLaughlin, F.A., and Timmermans, M.-L., Deterioration of perennial sea ice in the Beaufort Gyre from 2003 to 2012 and its impact on the oceanic freshwater cycle, J. Geophys. Res. Oceans, 119, 1271–1305, doi: 10.1002/2013JC008999, 2014.

Kulikov, E.A., Carmack, E.C., and Macdonald, R.W., Flow variability at the continental shelf break of the Mackenzie Shelf in the Beaufort Sea, J. Geophys. Res., 103(C6), 12,725–12,741, doi: 10.1029/97JC03690, 1998.

Kwok, R., Cunningham, G.F., Zwally, H.J., and Yi, D., Ice, Cloud, and land Elevation Satellite (ICESat) over Arctic sea ice: Retrieval of freeboard, J. Geophys. Res., 112, C12013, doi: 10.1029/2006JC003978, 2007.

Kwok, R., Cunningham, G.F., Wensnahan, M., Rigor, I., Zwally, H.J., and Yi, D., Thinning and volume loss of the Arctic Ocean sea ice cover: 2003–2008, J. Geophys. Res., 114, C07005, doi: 10.1029/2009JC005312, 2009.

La, H.S., Shimada, K., Yang, E.J., Cho, K.-H., Ha, S.-Y., Jung, J., Min, J.-O., Kang, S.-H., and Ha, H.K., Further evidence of diel vertical migration of copepods under Arctic sea ice during summer, Mar. Ecol. Prog. Ser., 592, 283–289, doi: 10.3354/meps12484, 2018.

La, H.S., Ha, H.K., Kang, C.Y., Wåhlin, A.K., and Shin, H.C., Acoustic backscatter observations with implications for seasonal and vertical migrations of the zooplankton and nekton in the Amundsen shelf (Antarctica), Estuarine, Coastal and Shelf Sci., 152, 124-133, doi: 10.1016/j.ecss.2014.11.020, 2015.

Last, K.S., Hobbs, L., Berge, J., Brierley, A.S., and Cottier, F., Moonlight drives ocean-scale mass vertical migration of the zooplankton during the Arctic Winter, Curr. Biol., 26(2), 244–251, doi: 10.1016/j.cub.2015.11.038, 2016.

Leise, T.L., Indic, P., Paul, M.J., and Schwartz, W.J., Wavelet meets actogram, J. Biol. Rhythms, 28(1), 62–68, doi: 10.1177/0748730412468693, 2013.

Lemon, D.D., Gower, J.F.R., and Clarke, M.R., The acoustic water column profiler: a tool for long-term monitoring of zooplankton populations, In: MTS/IEEE Oceans 2001. An Ocean Odyssey, Conference Proceedings (IEEE Cat. No.01CH37295), Honolulu, HI, USA, pp. 1904-1909, vol.3, doi: 10.1109/OCEANS.2001.968137, 2001.

Lemon, D.D., Billenness, D., and Buermans, J., Comparison of acoustic measurements of zooplankton populations using an Acoustic Water Column Profiler and an ADCP, In: OCEANS 2008, Quebec City, QC, pp. 1-8, doi: 10.1109/OCEANS.2008.5152009, 2008.

Lemon, D., Johnston, P., Buermans, J., Loos, E., Borstad, G., and Brown, L., Multiple-frequency moored sonar for continuous observations of zooplankton and fish, In: 2012 Oceans, Hampton Roads, VA, pp. 1-6, doi: 10.1109/OCEANS.2012.6404918, 2012.

Liu, Y., and Key, J.R., Assessment of Arctic Cloud Cover Anomalies in Atmospheric Reanalysis Products Using Satellite Data, J. Climate, 29, 6065-6083, doi: 10.1175/JCLI-D-15-0861.1, 2016.

Lorke, A., Mcginnis, D.F., Spaak, P., and Wüest, A., Acoustic observations of zooplankton in lakes using a Doppler current profiler, Freshw. Biol., 49, 1280–1292, doi: 10.1111/j.1365-2427.2004.01267.x, 2004.

Marcus, N.H., and Scheef, L.P., Photoperiodism in Copepods, in Photoperiodism: The Biological Calendar, edited by Nelson, R.J., Denlinger, D.L., and Sommers, D.E., pp. 193–217, Oxford University Press, Oxford, U. K., 2009.

Madsen, K.S., Rasmussen, T.A.S., Ribergaard, M.H., and Ringgaard, I.M., High resolution sea ice modelling and validation of the Arctic with focus on south Greenland waters, 2004-2013, Polarforschung, 85(2), 101-105, doi: 10.2312/polfor.2016.006, 2015.

Markus, T. and Cavalieri, D., Snow Depth Distribution over Sea Ice in the Southern Ocean from Satellite Passive Microwave Data. In: Antarctic Sea Ice: Physical Processes, Interactions, and Variability, Antarctic Research Series, 74, 19-39. Washington, DC: American Geophysical Union, 1998.

Melling, H., Riedel, D.A., and Gedalof, Z., Trends in the draft and extent of seasonal pack ice, Canadian Beaufort Sea, Geophys. Res. Lett., 32, L24501, doi:10.1029/2005GL024483, 2005.

O'Brien, M.C., Melling, H., Pedersen, T.F., and Macdonald, R.W., The role of eddies and energetic ocean phenomena in the transport of sediment from shelf to basin in the Arctic, J. Geophys. Res., 116, C08001, doi: 10.1029/2010JC006890, 2011.

Ott, M.J., The accuracy of acoustic vertical velocity measurements: instrument biases and the effect of Zooplankton migration, Continental Shelf Research, 25, 243-257, doi: 10.1016/j.csr.2004.09.007, 2005.

Perovich, D.K., The optical properties of sea ice, CRREL Monogr., 96-1, 25, 1996.

Petrusevich, V.Y., Dmitrenko, I.A., Niemi, A., Kirillov, S.A., Kamula, C.M., Kuzyk, Z.Z.A., Barber, D.G., and Ehn, J.K., Impact of tidal dynamics on diel vertical migration of zooplankton in Hudson Bay, Ocean Science, 16, 337–353, doi: 10.5194/os-16-337-2020, 2020.

Petrusevich, V., Dmitrenko, I.A., Kirillov, S.A., Rysgaard, S., Falk-Petersen, S., Barber, D.G., Boone, W., and Ehn, J.K., Wintertime water dynamics and moonlight disruption of the acoustic backscatter diurnal signal in an ice-covered Northeast Greenland fjord, J. Geophys. Res. Oceans, 121, 4804–4818, doi: 10.1002/2016JC011703, 2016.

Pickart, R.S., Shelfbreak circulation in the Alaskan Beaufort Sea: Mean structure and variability, J. Geophys. Res., 109, C04024, doi: 10.1029/2003JC001912, 2004.

Pickart, R.S., Weingartner, T.J., Pratt, L.J., Zimmermann, S., and Torres, D.J., Flow of winter-transformed Pacific water into the western Arctic, Deep Sea Res., Part II, 52, 3175–3198, doi: 10.1016/j.dsr2.2005.10.009, 2005.

Pnyushkov, A., Polyakov, I.V., Padman, L., and Nguyen, A.T., Structure and dynamics of mesoscale eddies over the Laptev Sea continental slope in the Arctic Ocean, Ocean Sci., 14, 1329-1347, doi: 10.5194/os-14-1329-2018, 2018.

Poulin, E., Palma, A.T., Leiva, G., Narvaez, D., Pacheco, R., Navarrete, S.A., and Castilla, J.C., Avoiding offshore transport of competent larvae during upwelling events: The case of the gastropod Concholepas concholepas in Central Chile, Limnol. Oceanogr., 47(4), 1248–1255, doi: 10.4319/lo.2002.47.4.1248, 2002a.

Poulin, E., Palma, A.T., Leiva, G., Hernández, E., Martínez, P., Navarrete, S.A., and Castilla, J.C., Temporal and spatial variation in the distribution ofepineustonic competent larvae of *Concholepas concholepas* along the central coast of Chile, Mar. Ecol. Prog. Ser., 229, 95–104, doi: 0.3354/meps229095, 2002b.

Queiroga, H., Cruz, T., dos Santos, A., Dubert, J., Gonzalez-Gordillo, J.I., Paula, J., Peliz, A., and Santos, A.M.P., Oceanographic and behavioural processes affectinginvertebrate larval dispersal and supply in the westernIberia upwelling ecosystem, Progress in Oceanography, 74, 174–19, doi: 10.1016/j.pocean.2007.04.007, 2007.

Shanks, A.L., and Brink, L., Upwelling, downwelling, and cross-shelf transportof bivalve larvae: test of a hypothesis, Mar. Ecol. Prog. Ser., 302: 1–12, doi: 10.3354/meps302001, 2005.

Spreen, G., Kaleschke, L., and Heygster, G., Sea ice remote sensing using AMSR-E 89 GHz channels, J. Geophys. Res., 113, C02S03, doi: 10.1029/2005JC003384, 2008.

Schweiger, A., Lindsay, R., Zhang, J., Steele, M., Stern, H., Uncertainty in modeled arctic sea ice volume, J. Geophys. Res., doi: 10.1029/2011JC007084, 2011

Spall, M., Pickart, R., Fratantoni, P., and Plueddemann, A., Western Arctic shelfbreak eddies: Formation and transport, J. Phys. Oceanogr., 38, 1644–1668, doi: 10.1175/2007JPO3829.1, 2008.

Stanton, T.K., Wiebe, P.H., Chu, D., Benfield, M.C., Scanlon, L., Martin, L., and Eastwood, R.L., On acoustic estimates of zooplankton biomass, ICES J. Mar. Sci., 51(4), 505–512, doi: 10.1006/jmsc.1994.1051, 1994.

Sun H., Hendry, D.C., Player, M.A. and Watson, J., In Situ Underwater Electronic Holographic Camera for Studies of Plankton, IEEE Journal of Oceanic Engineering, 32(2), 373–382, doi: 10.1109/JOE.2007.891891, 2007.

Tran, D., Sow, M., Camus, L., Ciret, P., Berge, J., and Massabuau, J.-C., In the darkness of the polar night, scallops keep on a steady rhythm, Sci. Reports, 6, 32435, doi: 10.1038/srep32435, 2016.

van Haren, H., and Compton, T.J., Diel Vertical Migration in Deep Sea Plankton Is Finely Tuned to Latitudinal and Seasonal Day Length, PLoS One, 8(5), e64435, doi: 10.1371/journal.pone.0064435, 2013.

Vestheim, H., Røstad, A., Klevjer, T.A., Solberg, I., and Kaartvedt, S., Vertical distribution and diel vertical migration of krill beneath snow-covered ice and in ice-free waters, J. Plankton Res., 36(2), 503–512, doi: 10.1093/plankt/fbt112, 2014.

Wallace, M.I., Cottier, F.R., Berge, J., Tarling, G.A., Griffiths, C., and Brierley, A.S., Comparison of the zooplankton vertical migration in an ice-free and a seasonally ice-covered Arctic fjord: An insight into the influence of sea ice cover on the zooplankton behavior, Limnol. Oceanogr., 55(2), 831–845, doi: 10.4319/lo.2010.55.2.0831, 2010.

Wang, H., Chen, H., Xue, L., Liu, N., and Liu, Y., The zooplankton diel vertical migration and influence of upwelling on the biomass in the Chukchi Sea during summer, Acta Oceanologica Sinica, 34(5), 68–74, doi: 10.1007/s13131-015-0668-x, 2015.

Wang, X., Key, J., Kwok, R., and Zhang, J., Comparison of Arctic Sea Ice Thickness from Satellites, Aircraft, and PIOMAS Data, Remote Sens., 8, 713, doi: 10.3390/rs8090713, 2016.

Webster, C., Varpe, Ø., Falk-Petersen, S., Berge, J., Stübner, E., and Brierley, A., Moonlit swimming: Vertical distributions of macrothe zooplankton and nekton during the polar night, Polar Biol., 38(1), 75–85, doi: 10.1007/s00300-013-1422-5, 2015.

Weingartner, T., Cavalieri, D., Aagaard, K., and Sasaki, Y., Circulation, dense water formation, and outflow on the northeast Chukchi shelf, J. Geophys. Res., 103(C4), 7647–7661, doi: 10.1029/98JC00374, 1998.

Williams, W.J., Carmack, E.C., Shimada, K., Melling, H., Aagaard, K., Macdonald, R.W., and Ingram, R.G., Joint effects of wind and ice motion in forcing upwelling in Mackenzie Trough, Beaufort Sea, Cont. Shelf Res., 26, 2352–2366, doi: 10.1016/j.csr.2006.06.012, 2006.

Wood, T.M., and Gartner, J.W., Use of Acoustic Backscatter and Vertical Velocity to Estimate Concentration and Dynamics of Suspended Solids in Upper Klamath Lake, South-Central Oregon: Implications for Aphanizomenon flos-aquae, Scientific Investigations Report 2010–5203, U.S. Geological Survey, Reston, Virginia, 20 p., 2010.

Woodgate, R.A., Aagaard, K., and Weingartner, T.J., Monthly temperature, salinity, and transport variability of the Bering Strait through flow, Geophys. Res. Lett., 32, L04601, doi: 10.1029/2004GL021880, 2005.

Yi, D., and Zwally, H.J., Arctic Sea Ice Freeboard and Thickness, Version 1. Boulder, Colorado USA. NASA National Snow and Ice Data Center Distributed Active Archive Center, doi: 10.5067/SXJVJ3A2XIZT. 2009, updated 2014.

Zhang, J.L. and Rothrock, D.A., Modeling global sea ice with a thickness and enthalpy distribution model in generalized curvilinear coordinates“, Mon. Weather Rev., 131, 845-861, doi: 10.1175/1520-0493(2003)131<0845:MGSIWA>2.0.CO;2, 2003.

Figures

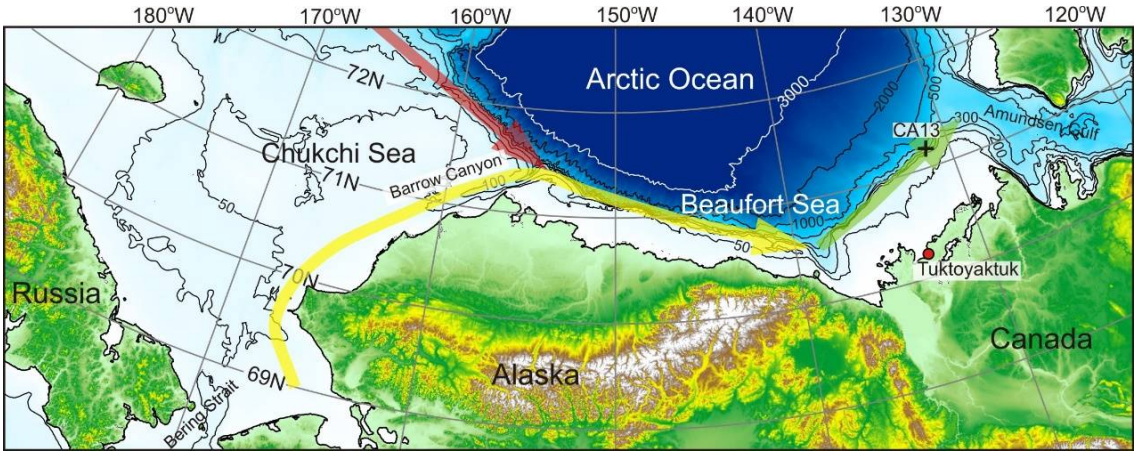

Figure 1: Map of the Beaufort Sea with the location of the ArcticNet mooring CA13 (black numbered cross). Thick red, yellow, and green arrows show circulation associated with the shelfbreak jet over the Chukchi Sea and western and eastern Beaufort Sea, respectively.

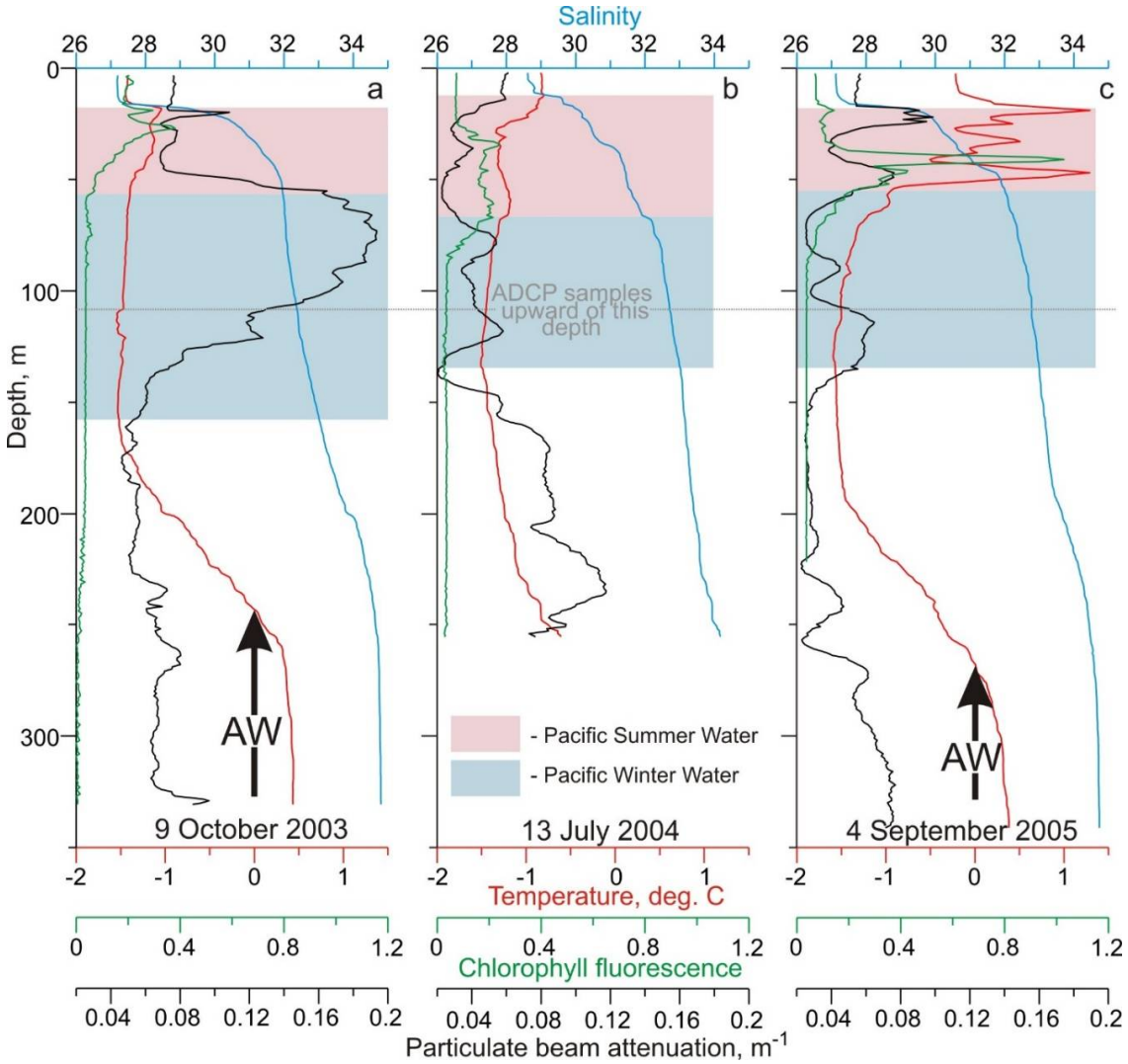

945 **Figure 2:** Vertical temperature (red), salinity (blue), chlorophyll fluorescence (green) and particulate beam attenuation (black) profiles taken at (**a**) mooring deployment on 9 October 2003, (**b**) on 13 July 2004 and (**c**) at mooring recovery on 4 September 2005. Pink and blue shading and black arrows highlight Pacific Summer Water (PSW), Pacific Winter Water (PWW), and Atlantic Water (AW), respectively, following Dmitrenko et al. (2016).

950

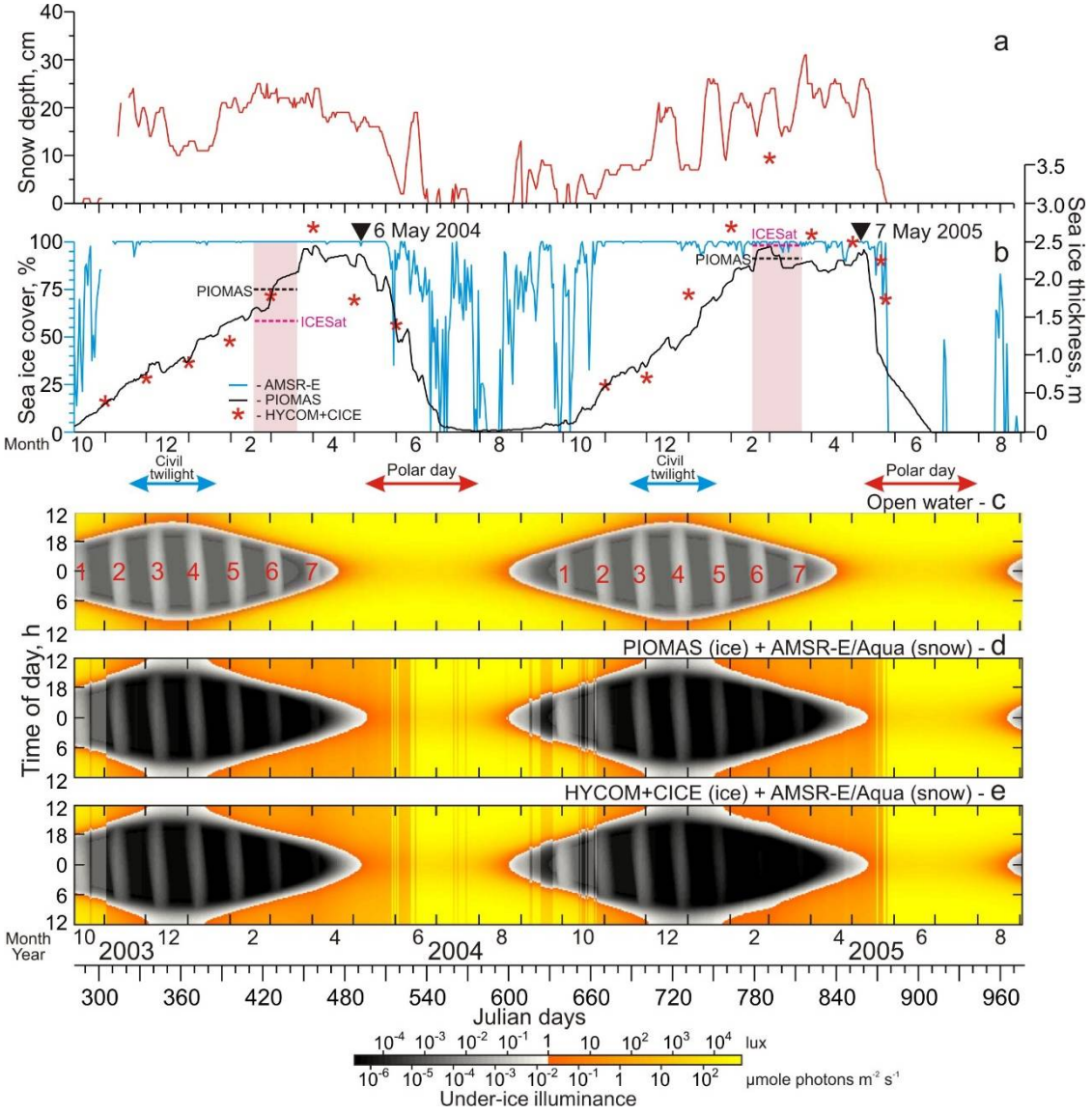

Figure 3: Time series of the (**a**) snow depth (cm, red), and (**b**) sea-ice concentrations (%, blue) and thickness (m) from PIOMAS (black) and HYCOM+CICE (red stars). (**b**) Pink shedding highlights periods of two ICESat campaigns. Black and purple horizontal segments indicate the mean sea-ice thickness derived from PIOMAS and ICESat, respectively. Black triangles at the top identify the time when the RADARSAT satellite images in Figure 6 were acquired. (**c-e**) Actograms of under-ice illuminance modeled for (**c**) open water conditions, (**d,e**) snow from AMSR-E/Aqua, and sea-ice thickness from (**d**) PIOMAS and (**e**) HYCOM+CICE. Red and blue arrows at the top indicate the polar day and civil twilight, respectively. (**c**) Red numbers reference the full moon occurrences.

965

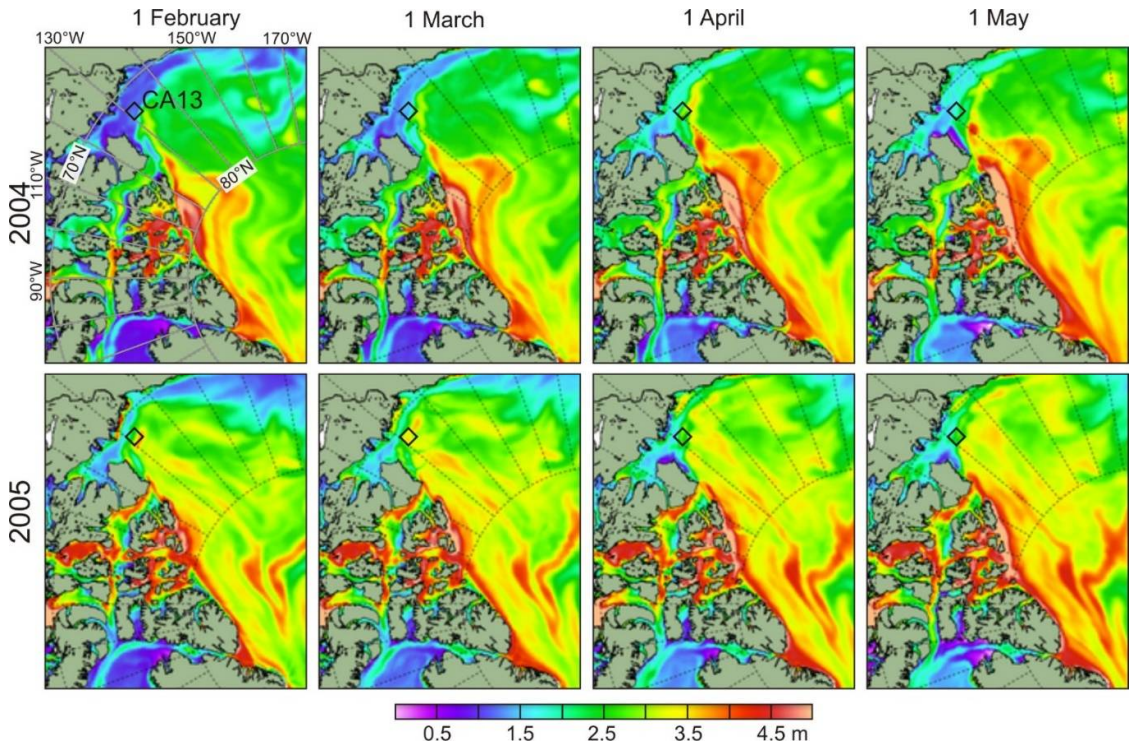

970 **Figure 4**: Spatial distribution of sea-ice thickness (m) based on model simulations using DMI's ocean and sea ice model HYCOM+CICE for February-May 2004 (top) and 2005 (bottom). The black diamonds depict mooring position.

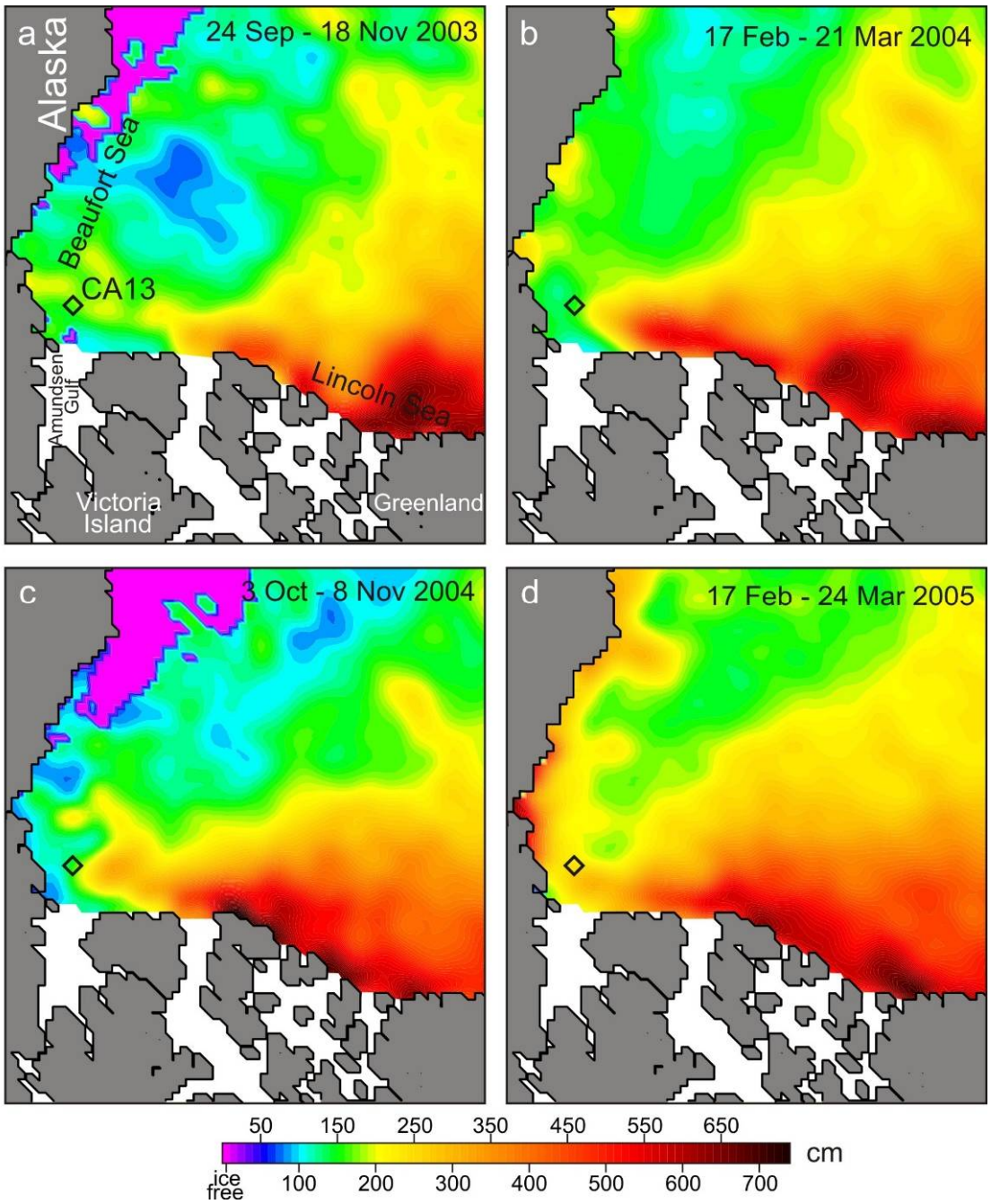

Figure 5: Spatial distribution of sea-ice thickness (cm) over the Canada Basin compiled using gridded sea ice thickness data from ICESat campaigns for (**a**) 24 September – 18 November 2003, (**b**) 17 February – 21 March 2004, (**c**) 3 October – 8 November 2004 and (**d**) 17 February – 24 March 2005 following Kwok et al. (2009). The black diamonds depict mooring position.

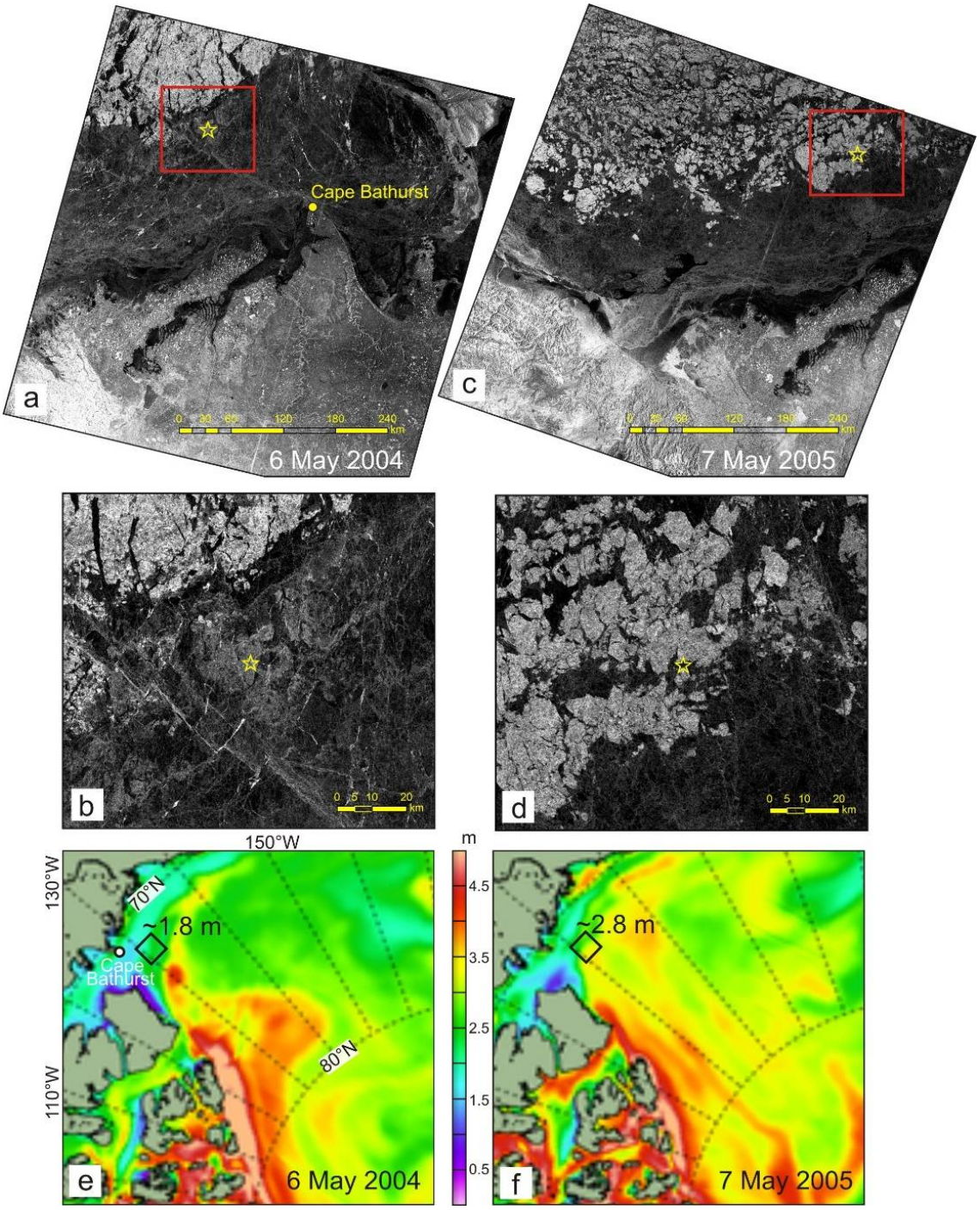

Figure 6: (**a-d**) RADARSAT satellite images taken before sea-ice breakup over the CA13 location northeast of Cape Bathurst on (**a**) 6 May 2004 and (**c**) 7 May 2005. Red rectangles show mooring region enlarged in **b** and **d**. Yellow stars depict mooring position. The dark areas are associated with the first-year pack ice (< 2 m thick). The lighter areas indicate the multi-year pack ice (> 2 m thick). (**e-f**) Spatial distribution of sea-ice thickness (m) based on the HYCOM+CICE model simulations for (**e**) 6 May 2004 and (**f**) 7 May 2005. The black diamonds depict mooring position. Numbers show approximate sea-ice thickness.

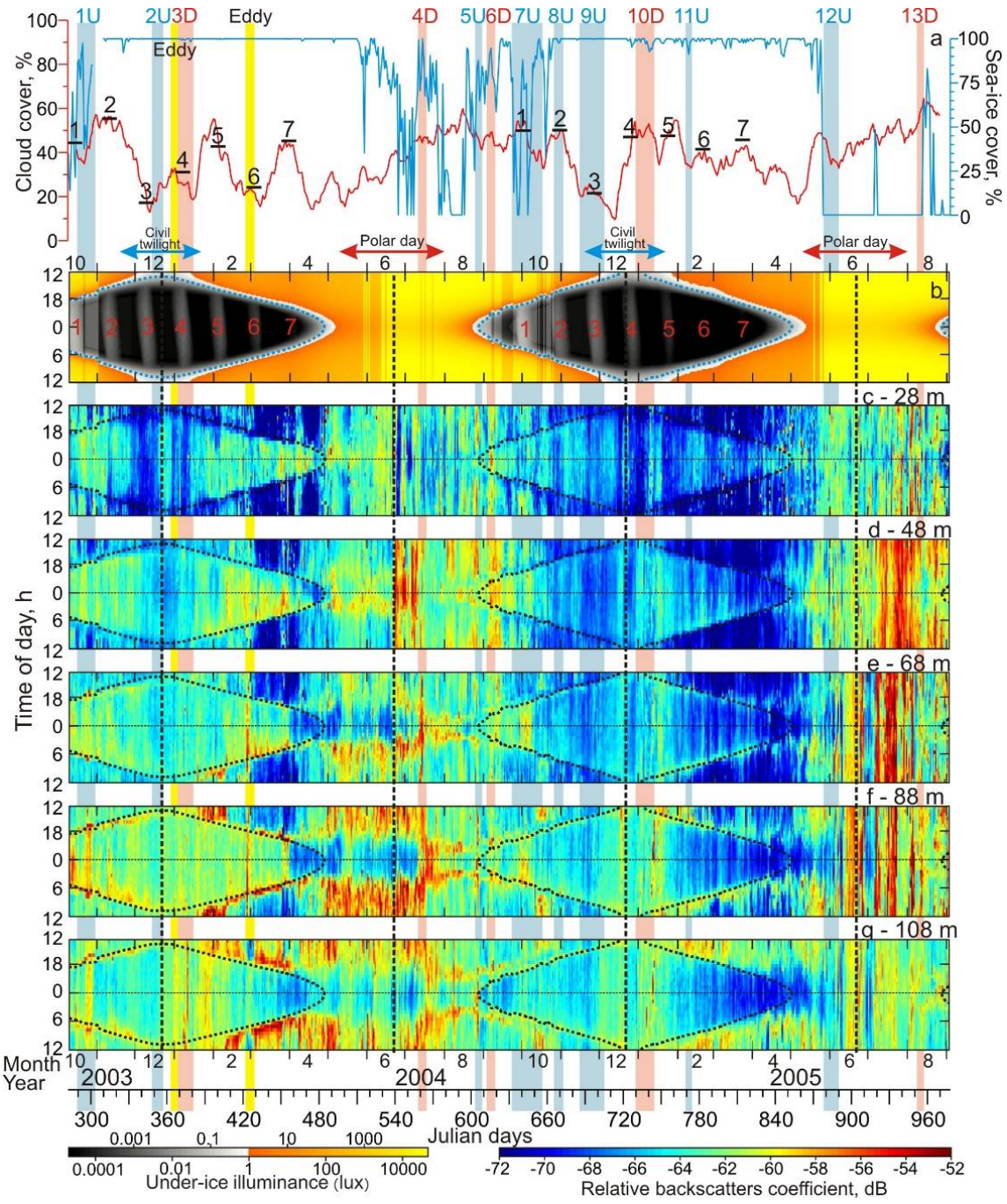

Figure 7: (**a**) Time series of sea-ice concentrations (blue, %) and 15-day running mean of total cloud cover (red, %). Actograms of (**b**) modeled under-ice illuminance (lux) based on HYCOM+CICE sea-ice thickness, and (**c**-**g**) MVBS (dB) at five depth levels: (**c**) 28 m, (**d**) 48 m, (**e**) 68 m, (**f**) 88 m, and (**g**) 108 m. The dotted blue (**b**) and black (**c**-**g**) lines depicts 0.1-lux threshold. Red and blue arrows at the top indicate the polar day and civil twilight, respectively. Red numbers reference the full moon occurrences, and black horizontal segments in (**a**) indicate the mean cloud cover for these periods. Black dashed vertical lines depict solstices. Red and blue shading highlight the downwelling (D) and upwelling (U) events, respectively, with their reference numbers on the top. Yellow shading highlights eddies.

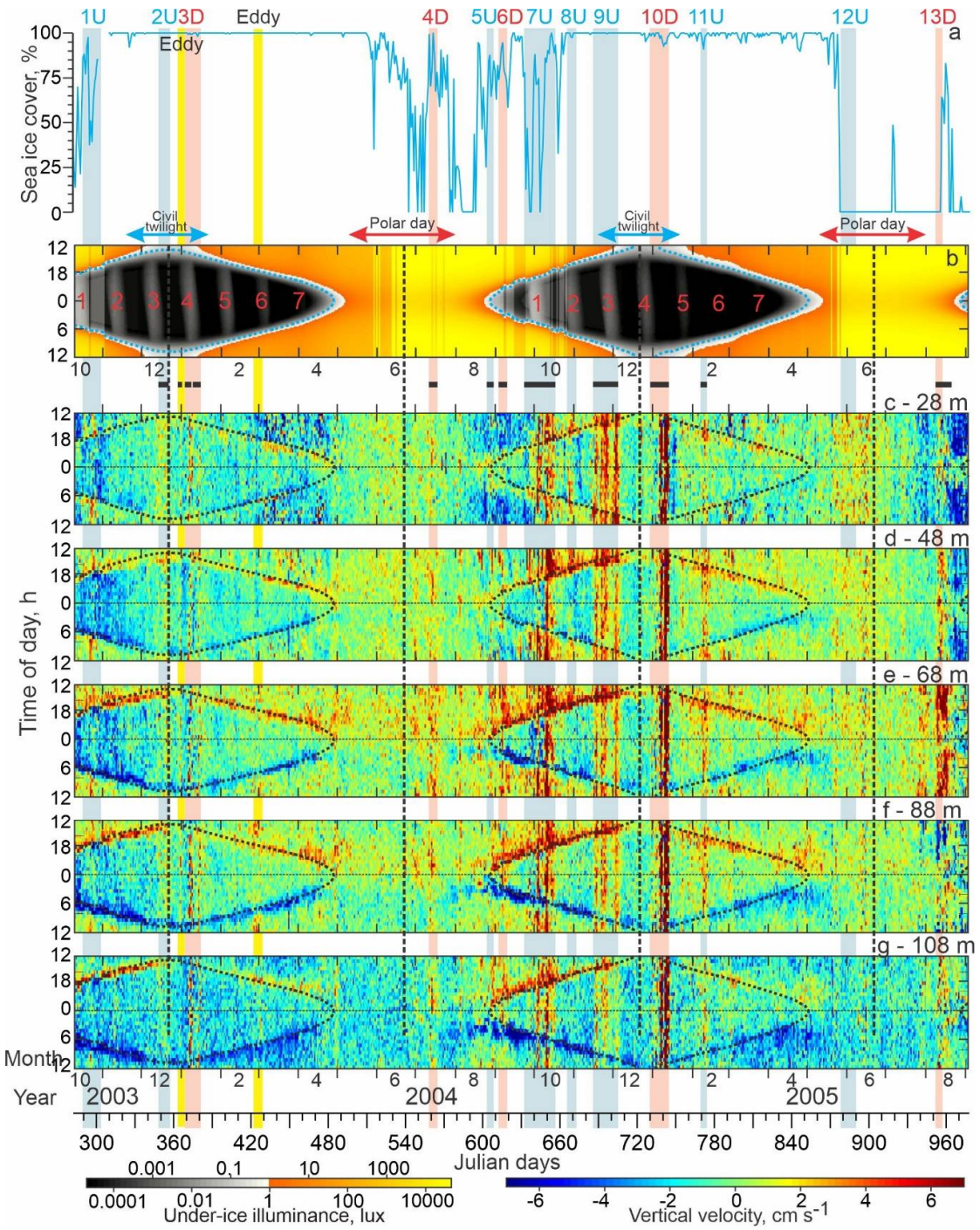

Figure 8: (**a**) Time series of sea-ice concentrations (%). Actograms of (**b**) modeled under-ice illuminance (lux) based on HYCOM+CICE sea-ice thickness, and (**c**-**g**) ADCP-measured vertical velocity (cm s^{-1}) at five depth levels: (**c**) 28 m, (**d**) 48 m, (**e**) 68 m, (**f**) 88 m and (**g**) 108 m. Positive/negative values correspond to the upward/downward flow. Horizontal black lines at the top of panel (c) depict periods of noise in vertical velocity attributed to spatial inhomogeneity of the flow field and errors in the ADCP tilt angle (for more details see section 3). All other designations are similar to those in Figure 7.

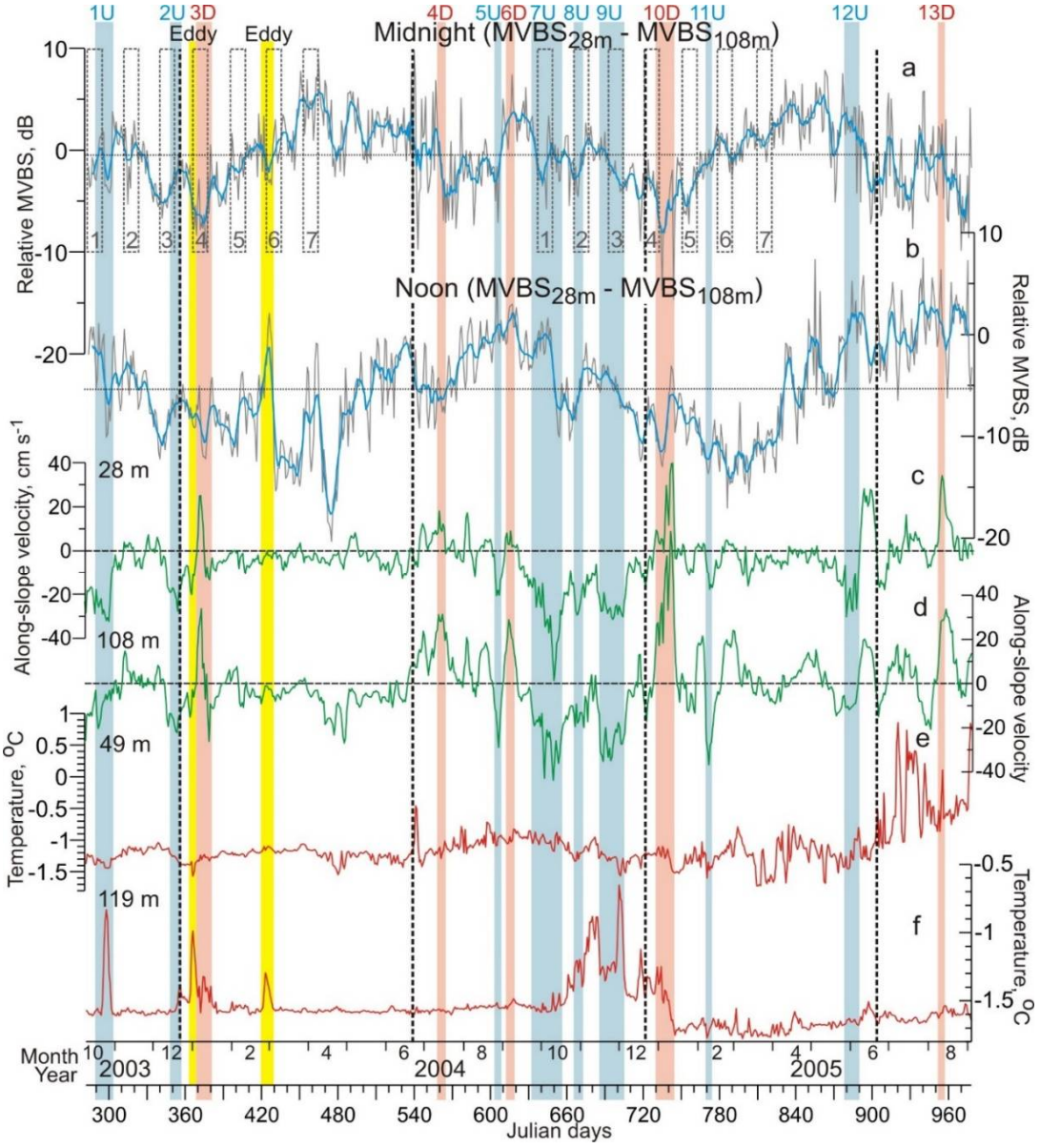

Figure 9: Time series of the daily mean relative MVBS (dB) from 28 m to 108 m depth for the astronomic (**a**) midnight and (**b**) noon ±1 h, along-slope (positive northeastward) velocity for depths of (**c**) 28 m and (**d**) 108 m (cm s^{-1}) and water temperatures (°C) for (**c**) 49 m and (**d**) 119 m depth. (**a**-**b**) Blue lines show the 7-day running mean. Horizontal dotted lines show the 2-year means. Positive/negative values correspond to MVBS gain/loss at 28/108 m depth. (**a**) Gray dashed rectangles depict the full moon occurrence ±6 days. All other designations are similar to those in Figure 7.

1025

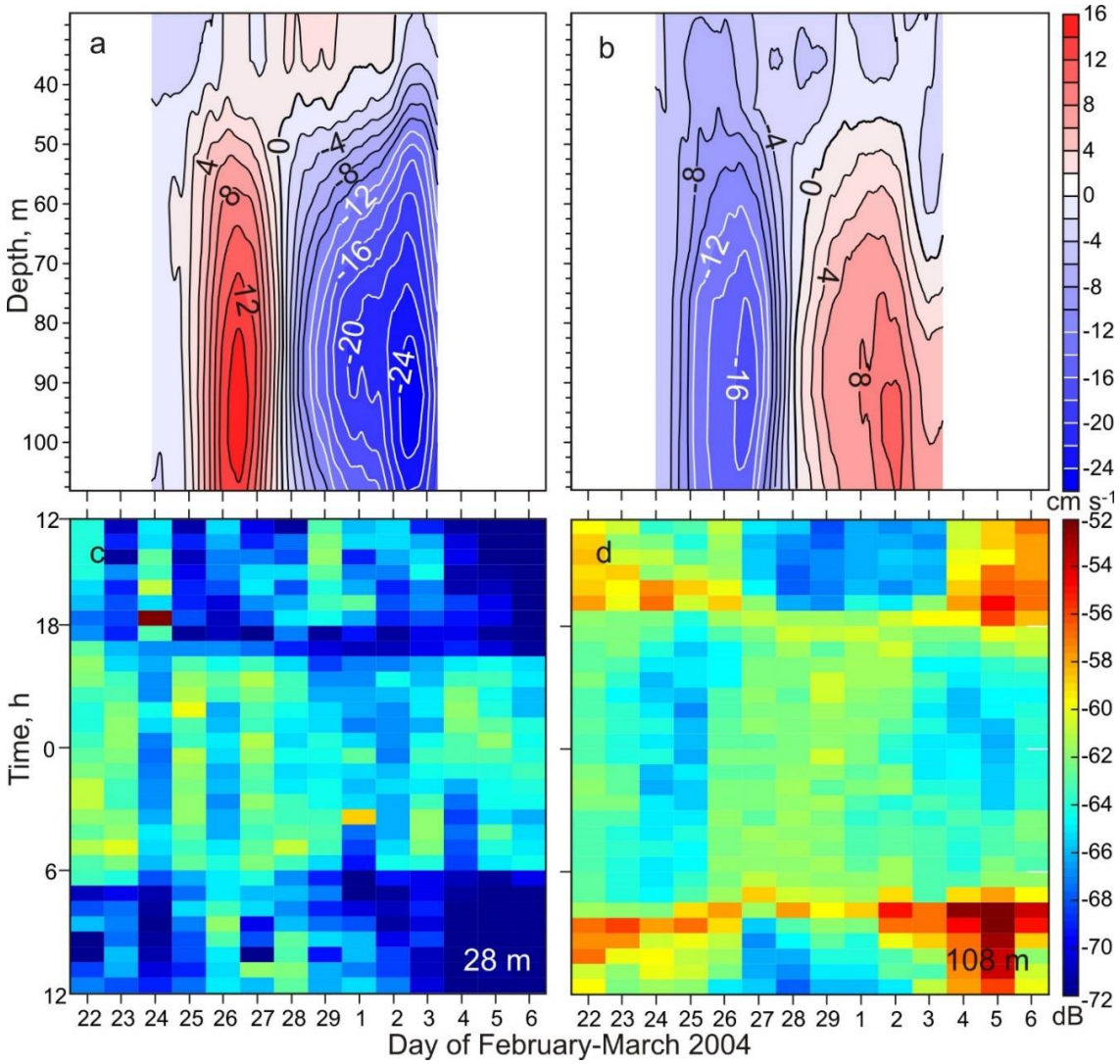

1030 **Figure 10**: Enlarged view of the February-March 2004 eddy. (**a)** Zonal and (**b**) meridional current (cm s^{-1}) records as functions of depth adopted from Dmitrenko et al. (2018). (**c-d**) actograms of MVBS (dB) for (**c**) 28m and (**d**) 108 m depth.

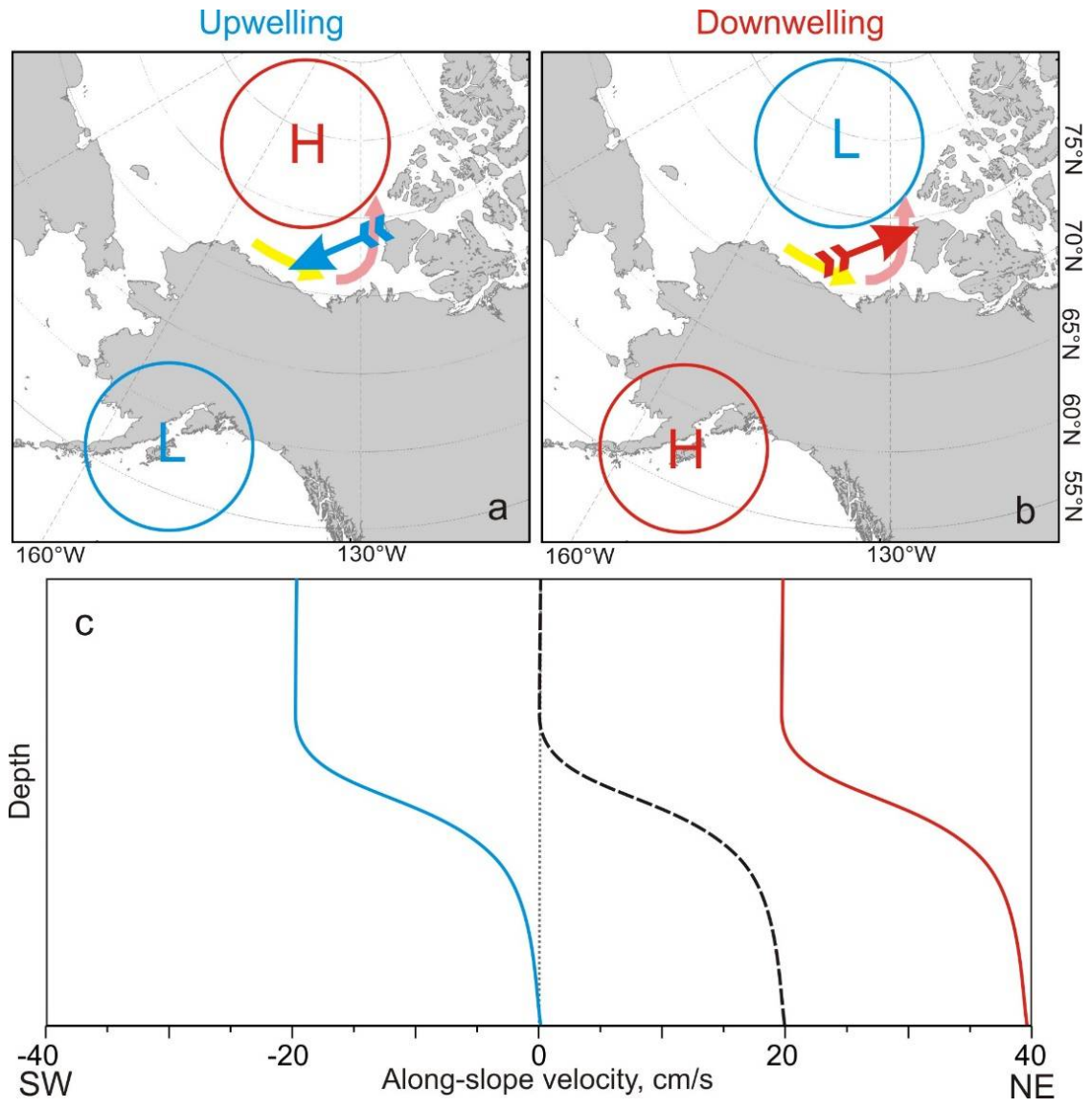

Figure 11: Schematic depiction showing atmospheric forcing for (**a**) upwelling and (**b**) downwelling along the eastern Beaufort Sea continental slope adopted from Kirillov et al. (2016). Blue and red arrows indicate geostrophic wind associated with concurrence between atmospheric low and high depicted by blue and red circles, respectively. Yellow and pink arrows show circulation with shelfbreak jet over the western and eastern Beaufort Sea, respectively, intensified by local downwelling. (**c**) Schematic depiction suggesting generation of the surface-intensified (blue curve) and depth-intensified (red curve) along-slope currents as a result of upwelling and downwelling, respectively, superimposed on the hypothetical bottom-intensified shelfbreak current (black dashed curve) following Dmitrenko et al. (2018).